Momentum Flux of Convective Gravity Waves Derived from an Offline Gravity Wave Parameterization. Part II: Impacts on the Quasi-Biennial Oscillation

MIN-JEE KANG AND HYE-YEONG CHUN

Department of Atmospheric Sciences, Yonsei University, Seoul, South Korea

YOUNG-HA KIM

Institut für Atmosphäre und Umwelt, Goethe Universität Frankfurt, Frankfurt, Germany

PETER PREUSSE AND MANFRED ERN

Stratosphere, Institute of Energy and Climate Research, Forschungszentrum Jülich, Jülich, Germany

(Manuscript received 22 March 2018, in final form 3 July 2018)

ABSTRACT

The characteristics of small-scale convective gravity waves (CGWs; horizontal wavelengths <100 km) and their contributions to the large-scale flow in the stratosphere, including the quasi-biennial oscillation (QBO), are investigated using an offline calculation of a source-dependent, physically based CGW parameterization with global reanalysis data from 1979 to 2010. The CGW momentum flux (CGWMF) and CGW drag (CGWD) are calculated from the cloud top (source level) to the upper stratosphere using a Lindzen-type wave propagation scheme. The 32-yr-mean CGWD exhibits large magnitudes in the tropical upper stratosphere and near the stratospheric polar night jet (~60°). The maximum positive drag is 0.1 (1.5) $\mathrm{m\,s^{-1}\,day^{-1}}$, and the maximum negative drag is -0.9 (-0.7) $\mathrm{m\,s^{-1}\,day^{-1}}$ in January (July) between 3 and 1 hPa. In the tropics, the momentum forcing by CGWs at 30 hPa associated with the QBO in the westerly shear zone is 3.5–6 $\mathrm{m\,s^{-1}\,month^{-1}}$, which is smaller than that by Kelvin waves, while that by CGWs in the easterly shear zone (3.1–6 $\mathrm{m\,s^{-1}\,month^{-1}}$) is greater than that by any other equatorial planetary waves or inertio-gravity waves (inertio-GWs). Composite analyses of the easterly QBO (EQBO) and westerly QBO (WQBO) phases reveal that the zonal CGWMF is concentrated near 10°N and that the negative (positive) CGWD extends latitudinally to ±20° (±10°) at 30 hPa. The strongest (weakest) negative CGWD is in March–May (September–November) during the EQBO, and the strongest (weakest) positive CGWD is in June–August (March–May) during the WQBO. The CGWMF and CGWD are generally stronger during El Niño than during La Niña in the equatorial region.

1. Introduction

Vertically propagating gravity waves (GWs) transfer their momentum to large-scale flow in the middle atmosphere, where they dissipate (Lindzen 1981; Holton 1983). The GWs in the current resolution of general circulation models (GCMs) are not fully resolved, and thus, their effects must still be parameterized in GCMs (Kim et al. 2003). It is well known that updrafts in summer polar region and downdrafts in winter polar region (i.e., one-cell meridional gyre) in the mesosphere are driven by positive (negative) GW momentum forcing in the summer (winter) hemisphere, and adiabatic cooling and heating by the updraft and downdraft, respectively, cause significant deviations in the mesospheric temperature from the radiative equilibrium temperature (Andrews et al. 1987; Fritts and Alexander 2003; Kim et al. 2003). Among the various sources of GWs, convection can generate high-frequency GWs (Lane et al. 2001; Song et al. 2003). Therefore, convective GWs (CGWs) have a broad phase speed spectrum and can propagate to higher altitudes without seasonal restrictions. In the tropical stratosphere, CGWs can significantly contribute to the evolution of the quasi-biennial oscillation (QBO) and semiannual oscillation (SAO; e.g.,

---

Supplemental information related to this paper is available at the Journals Online website: https://doi.org/10.1175/JAS-D-18-0094.s1.

Corresponding author: Prof. Hye-Yeong Chun, chunhy@yonsei.ac.kr

DOI: 10.1175/JAS-D-18-0094.1

Alexander and Holton. 1997; Garcia et al. 1997; Song et al. 2007). In addition, the momentum forcing by CGWs in driving the Brewer–Dobson circulation is comparable to that by orographic GWs in a GCM simulation (Chun et al. 2011). CGWs contribute to stratospheric circulation not only in the tropical region but also in the polar region. Choi and Chun (2013) demonstrated that an excessive polar night jet and cold-pole biases in the Southern Hemisphere (SH) stratosphere during the wintertime that have been a long-lasting problem in GCM simulations can be alleviated significantly by including a CGW parameterization into a GCM.

Among the aforementioned phenomena related to CGWs in the stratosphere, the QBO in the tropical stratosphere is perhaps most directly related to CGWs. The QBO is a dominant variability in the zonal-mean zonal wind in the tropical stratosphere with a period of approximately 20–35 months (Baldwin et al. 2001). It is internally generated through momentum deposition by vertically propagating equatorial planetary and gravity waves (Lindzen and Holton 1968; Holton and Lindzen 1972) and partly by laterally propagating extratropical Rossby waves (Dunkerton 1997; O'Sullivan 1997). The QBO has long been one of few phenomena that could not be simulated by GCMs. Recently, however, several climate models have internally simulated a QBO with "well tuned" nonorographic GW parameterizations (e.g., Scaife et al. 2000; Orr et al. 2010; Xue et al. 2012; Kim et al. 2013; Krismer and Giorgetta 2014; Schirber et al. 2014; Kim and Chun 2015a). However, simulating a realistic QBO in a climate model is still an ongoing issue (Butchart et al. 2018), since the conditions for a successful simulation of the QBO are highly dependent on the model based on its ability to generate realistic equatorial planetary waves at model grids and on the GW parameterizations used in the model.

To quantify the contribution of each wave type to the QBO, there have been several attempts to estimate the momentum forcing required to drive the QBO by equatorial planetary waves and GWs using observational data (Ern and Preusse 2009; Ern et al. 2014), reanalysis data (Ern et al. 2014; Kim and Chun 2015b), and modeling results (Giorgetta et al. 2006; Kawatani et al. 2010; Evan et al. 2012; Kim and Chun 2015a; Butchart et al. 2018). Although the results from those studies differ from one another, they have commonly revealed that the contributions of inertio-GWs and parameterized small-scale GWs (λ_h < 100–200 km, where λ_h is the horizontal wavelength) to the QBO evolution are significant. Ern et al. (2014) showed that the missing drag estimated from the ERA-Interim data (Dee et al. 2011) that is attributed mainly to GWs is generally larger than the planetary wave drag, especially in the easterly shear zone. The GW drag estimates ($\lambda_h > 100$ km) using High Resolution Dynamics Limb Sounder (HIRDLS) and Sounding of the Atmosphere using Broadband Emission Radiometry (SABER) satellite data are similar to those from ERA-Interim in the westerly shear zone but much smaller in the easterly shear zone.

More comprehensive analyses have been conducted for the contribution of each wave type to the QBO using modeling results. Kawatani et al. (2010) simulated a QBO-like oscillation with a mean period of 15 months using a high-resolution GCM with a horizontal resolution of a T213 spectral truncation (~60-km horizontal resolution) and showed that the main contributors to the QBO are GWs ($\lambda_h < 1000$ km), especially in the westerly to easterly transition. Evan et al. (2012) estimated the GW forcing using the Weather Research and Forecasting (WRF) Model with a horizontal grid spacing of 37 km and revealed that the GW forcing is ~60% (80%) of the total eastward (westward) forcing, of which small-scale GWs with $\lambda_h <$ 1000 km account for half. Recent high-resolution models, including those mentioned above, are useful tools for explicitly resolving GWs. However, GWs with horizontal wavelengths ranging from a few tens of kilometers to ~200 km, which can carry a large amount of momentum flux to the middle atmosphere and provide a significant amount of drag there when they dissipate, were not fully resolved by those models considering that the *effective* horizontal wavelength of the GCM simulation by Kawatani et al. (2010) was approximately 180 km and that the spectral power of GWs at horizontal wavelengths less than ~270 km was almost negligible in the WRF Model simulation by Evan et al. (2012).

Kim and Chun (2015a) successfully simulated the QBO using the Hadley Centre Global Environment Model, version 2 (HadGEM2; Martin et al. 2011), which includes the physically based CGW parameterization by Choi and Chun (2011) and background GW parameterization, and they assessed the contributions of GWs and equatorial planetary waves to the QBO. They showed that the positive momentum forcing by parameterized GWs is as large as that by Kelvin waves and that the negative momentum forcing by parameterized GWs is much larger than that of any other equatorial planetary waves in the lower stratosphere. The significant contribution of small-scale GWs to the QBO is well supported by Holt et al. (2016), who showed that a large portion of the QBO forcing is from parameterized GWs, even in a GCM with a 7-km resolution. Because they used a strong horizontal diffusion, which is common to stabilize mesoscale simulations, the *effective* horizontal wavelengths resolvable from the model become relatively longer, such as 6–10δ or 15–20δ (where δ is the horizontal grid spacing), depending on the dynamic core of a model (Skamarock 2004, 2011), and thus, CGWs with horizontal wavelengths shorter than 100 km are not likely resolved explicitly but needed for parameterization in their model. In addition, relatively low vertical resolution of their model, compared with the very fine horizontal resolution, likely leads to underestimation of both resolved planetary and gravity waves, requiring additional momentum forcing from parameterized GWs. Each GCM contains several systematic biases that lead to an underestimation in planetary waves and their momentum forcings (Richter et al. 2014); these uncertainties are associated with numerous factors, including the vertical/horizontal resolution, dynamical core of the model, and subgrid-scale parameterizations (Butchart et al. 2018). In particular, the large amount of unresolved momentum forcing or parameterized GW forcing required to simulate the QBO can be partly attributed to the coarse vertical resolution of the model, which leads to limitations in (i) the generation and dissipation of planetary waves with short vertical wavelengths such as Kelvin and mixed Rossby–gravity waves (Richter et al. 2014; Anstey et al. 2016) and (ii) the finding of wave breaking locations for GW parameterizations (Choi and Chun 2008).

While the contributions of GWs in the horizontal wavelength range of 200–1000 km have been investigated through observations and high-resolution GCM data, a significant contribution from small-scale GWs to the QBO has been estimated through the GCM output of GW parameterizations (e.g., Schirber et al. 2014; Kim and Chun 2015a). However, this estimation is highly dependent upon the model because the magnitude of GW forcing is inevitably tuned to yield the observed wind and temperature structures in a GCM. One way to overcome these drawbacks when estimating the small-scale CGW contribution to the driving of the QBO is to run a CGW parameterization offline for a long period of time in an atmospheric background provided by global reanalysis data. Of course, it must be ensured that the CGW parameterization simulates a realistic spectrum of GWs, and the magnitude should be constrained by proper observations.

Recently, Kang et al. (2017, hereafter Part I) made such an attempt using the offline version of a physically based and source-dependent CGW parameterization and hourly global reanalysis data with a horizontal resolution of 1° over 32 years (1979–2010). In Part I, the spatiotemporal characteristics of the cloud-top momentum flux (source spectrum) of the CGW parameterization were examined. The magnitude of the GW momentum flux was constrained by GW observations from superpressure balloons (SPBs) at $z \sim 19$ km in the tropical region from February to May 2010 (Jewtoukoff et al. 2013). Note that SPBs can detect a wide spectrum of GWs focusing on small-scale waves ($\lambda_h < 50$ km) for which we are interested in this study.

The amplitude and progression rate of the QBO are different for each QBO cycle. This is primarily caused by seasonal variations in convective activities in the tropical region and the resultant momentum forcing by the equatorial waves. The annual synchronization of the QBO cycle has been reported by several studies using observations (e.g., Dunkerton and Delisi 1985; Wallace et al. 1993) and reanalysis data (e.g., Huesmann and Hitchman 2001; Krismer et al. 2013; Taguchi and Shibata 2013). Taguchi and Shibata (2013) showed that the residual term of the transformed Eulerian-mean (TEM) equation, representing mostly GWs, in Japanese 25-year Reanalysis Project (JRA-25)/Japan Meteorological Agency Climate Data Assimilation System (JCDAS) data (Onogi et al. 2007) plays a major role in the seasonal cycle of the QBO. Another source of the variations in the QBO is El Niño–Southern Oscillation (ENSO). Taguchi (2010) showed that the QBO amplitude is larger during La Niña and that the descending shear rate is faster during El Niño using tropical radiosonde observations and empirical orthogonal function (EOF) analysis. The zonal-mean convective activities that are larger during El Niño than during La Niña lead to a larger zonal-mean GW momentum flux, and this may successively result in a faster phase progression rate of the QBO during El Niño, which had been shown from the modeled GWs with horizontal wavelengths ranging from 227 to 4447 km (Alexander et al. 2017) and parameterized GWs (Geller et al. 2016b). Extremely deep convection patterns are more frequently observed during La Niña in the tropical region, resulting in a broader spectrum of CGWs and a larger amplitude of QBO winds (Geller et al. 2016b; Alexander et al. 2017). Our convectively coupled and physically based GW offline parameterization data would be useful for investigating the GW forcing of the QBO given that the seasonal and interannual variations in convective activities and mean flows are considered in the present study.

In this study, we calculate the CGW momentum flux (CGWMF) and CGW drag (CGWD) in the stratosphere using the cloud-top momentum flux (CTMF) spectrum obtained from the offline CGW parameterization in Part I. The CGWs considered in this study are small-scale GWs with the dominant horizontal wavelengths less than 100 km. Based on this calculation, we first investigate the impact of the small-scale CGWs on large-scale flow in the stratosphere globally and then examine the impact on the QBO. This paper is organized as follows. Section 2 briefly describes the methodology and reanalysis data used for calculating the offline CGW parameterization data in the stratosphere. Then section 3 discusses the global characteristics of the CGWMF and CGWD in the stratosphere and compares the spectral shape of

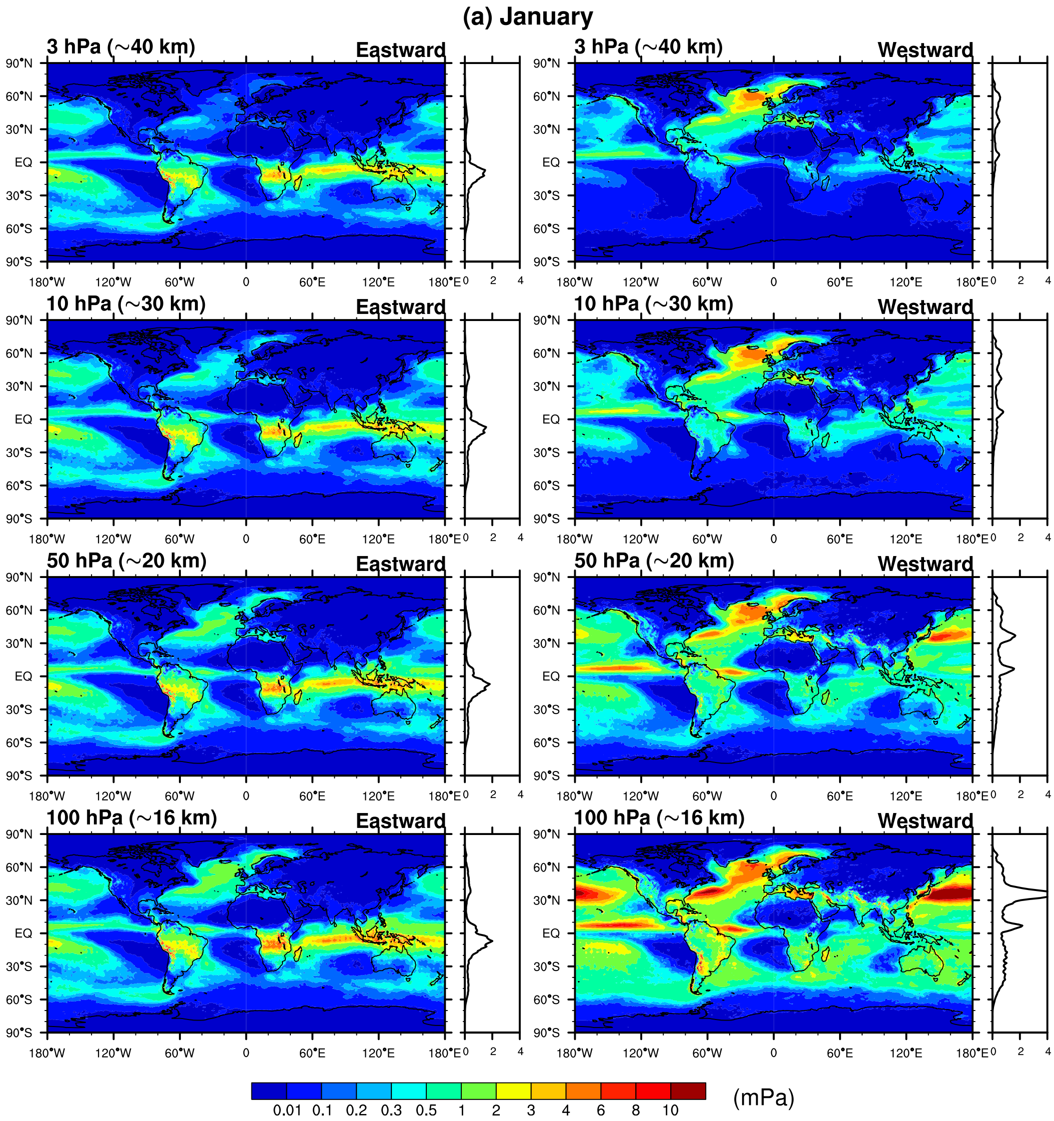

FIG. 1. Global distributions of the eastward and westward CGWMFs at (bottom to top) 100, 50, 10, and 3 hPa in (a) January and (b) July averaged from 1979 to 2010. The zonal-mean values are plotted to the right of each panel.

CGWMF with that observed from SPBs in the tropical region. Section 4 examines the contributions of CGWs to the driving of the QBO, and section 5 presents the characteristics of CGWs in the opposite phases of the QBO during different seasons and different ENSO phases. Summary and discussion of our results are given in the last section.

2. Data

In Part I, we investigated the spatiotemporal characteristics of the cloud-top (source level) momentum flux of CGWs based on a 32-yr calculation of an offline version of the CGW parameterization. The details of this CGW parameterization are given in Part I, but we will provide a brief description here. The CGW parameterization was first developed by Song and Chun (2005), who derived an analytic solution of the convective heating–induced GW momentum flux at the cloud top as a function of the phase speed. This parameterization was validated and updated by Choi and Chun (2011) using various mesoscale simulations with the ability to explicitly resolve CGWs. The parameterization was also compared with AIRS observations and showed a good agreement (Choi et al. 2012). In Part I, we further updated the Choi and Chun (2011) scheme by including nonlinear forcing effects within the CTMF formulation following the method by Chun et al. (2008). The inclusion of these effects into the CTMF formulation

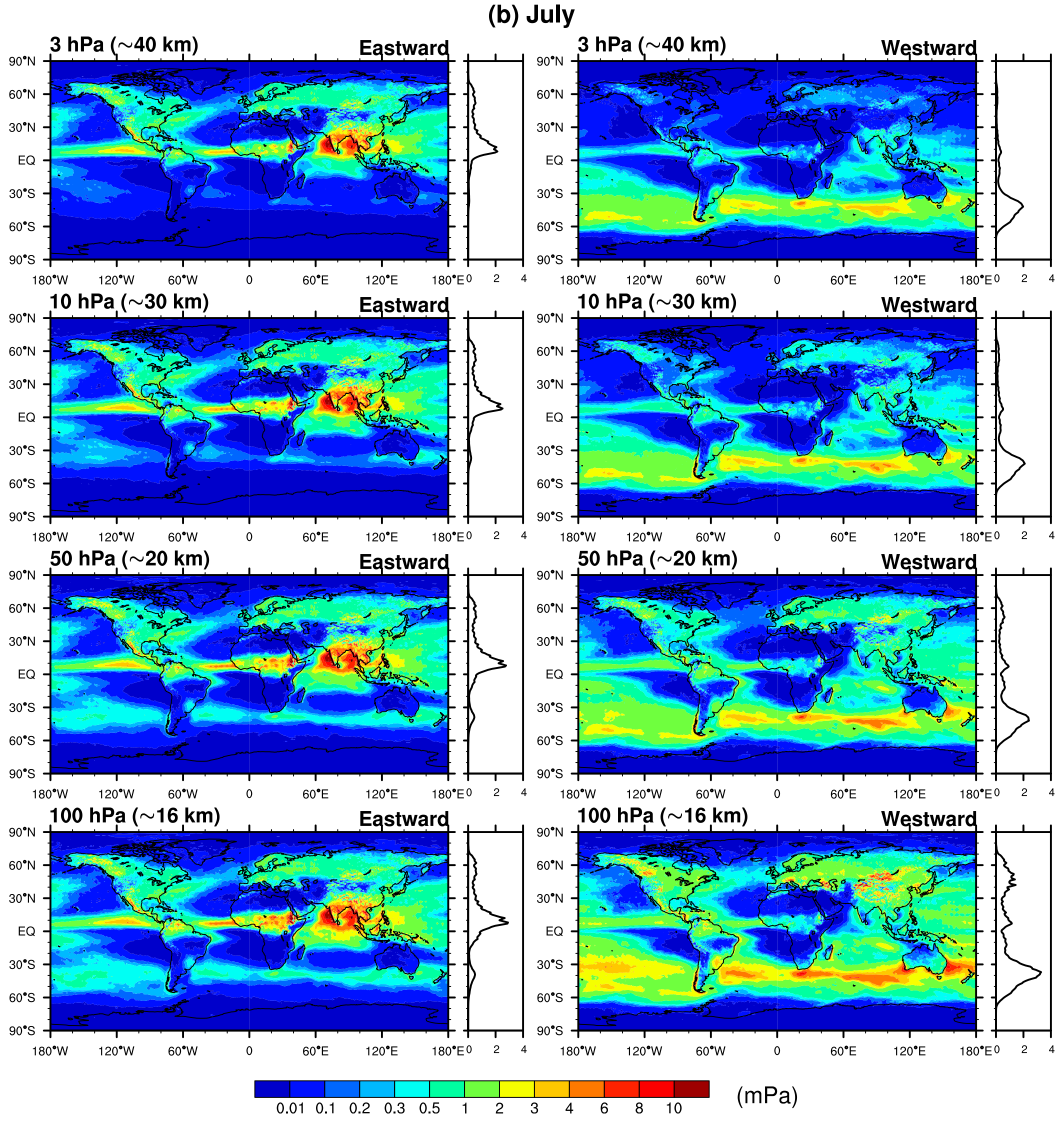

FIG. 1. (*Continued*)

is based on the fact that CGWs are generated not only by diabatic forcing but also by nonlinear forcing (Lane et al. 2001; Song et al. 2003; Chun et al. 2005; Choi et al. 2007). In the present study, we calculate the CGWMF and CGWD above the source level using the method of columnar wave propagation (Song and Chun 2006) based on Lindzen's linear saturation theory (Lindzen 1981). The CGWs are set to propagate in four directions, namely, 45°, 135°, 225°, and 315°, and the results are projected along the zonal and meridional directions. The global data used for the offline calculation are the NCEP Climate Forecast System Reanalysis (CFSR; Saha et al. 2010) over 32 years (1979–2010) with a horizontal resolution of 1° longitude by 1° latitude and a temporal resolution of 1 h (forecast fields). The same dataset was used in Part I. The hourly temporal resolution of the CFSR is especially attractive for properly representing the temporal variations in convective activities in the current study. It has been reported that the temporal variabilities in the tropical precipitation data of the CFSR are superior to those in other reanalysis data (Wang et al. 2012; Kim and Alexander 2013). The results utilized in the present study are composed of the CGWMF and CGWD in the stratosphere.

3. Global features of the CGWMF and CGWD in the stratosphere

Figure 1 shows the 32-yr-averaged eastward and westward CGWMF at the levels of 100, 50, 10, and 3 hPa.

Note that the sign of CGWMF is determined by the sign of $c - U$, which is shown in Eq. (1) of Part I (where c is the ground-based phase speed and U is the large-scale mean wind), and thus, eastward (westward) means eastward (westward) relative to the mean flow. The zonal-mean values are plotted on the right side of each panel. In January (Fig. 1a), there is a strong westward momentum flux in the winter hemisphere storm-track region (30°–50°N) at 100 hPa, as the background wind at the source level is westerly (see Fig. 3 of Part I). In the tropical region (10°N–20°S), an eastward momentum flux is dominant at 100 hPa, as the background wind at the source level is easterly, except in the western hemisphere between 0° and 10°N. As the altitude increases, the westward CGWMF in the storm-track region dissipates significantly, and thus, the peaks in the Pacific and Atlantic storm-track regions nearly disappear at an altitude of 10 hPa. In the upper stratosphere (i.e., 10 and 3 hPa), an eastward (westward) momentum flux exhibits noticeable peaks in the tropical region (the northern Atlantic and Norwegian coast). A strong GW momentum flux in the stratosphere over the North Atlantic and Norwegian coast dominated by westward waves has also been detected by satellite instruments (Ern et al. 2017) and by high-resolution European Centre for Medium-Range Weather Forecasts (ECMWF) data (Preusse et al. 2014). Jet–front systems are considered to be possible sources of these GWs (Hertzog et al. 2001; Preusse et al. 2014). The strong peaks of CGWs in Fig. 1a in the current study demonstrate that CGWs might also be excited by moist heating of the jet–front system, as also suggested by Wei and Zhang (2014) and Wei et al. (2016).

In July (Fig. 1b), similar latitudinal variations in the eastward and westward momentum fluxes are shown considering hemispheric seasonal changes. However, during the propagation from 100 to 3 hPa, the westward momentum flux in the storm-track region dissipates less than that in January. Additionally, the eastward momentum flux in the Asian summer monsoon (0°–30°N, 60°–120°E) is nearly unfiltered and propagates to 3 hPa. Some portion of the eastward momentum flux in the Asian summer monsoon region may contribute the positive momentum forcing required to drive the westerly phase of the SAO in the tropical upper stratosphere and lower mesosphere, considering that the momentum forcing by GWs can largely contribute to the westerly wind shear of the SAO (Ern et al. 2015). Another portion may propagate poleward in the mesosphere during the Northern Hemisphere (NH) summer, as shown in Sato et al. (2009), Ern et al. (2011), and Thurairajah et al. (2017). This implies that CGWs in this area can be a source of the positive drag forcing in the summer mesosphere required for driving the one-cell meridional gyre in the upper mesosphere that leads to a departure of the zonal-mean zonal temperature from the radiative equilibrium temperature (Andrews et al. 1987; Fritts and Alexander 2003).

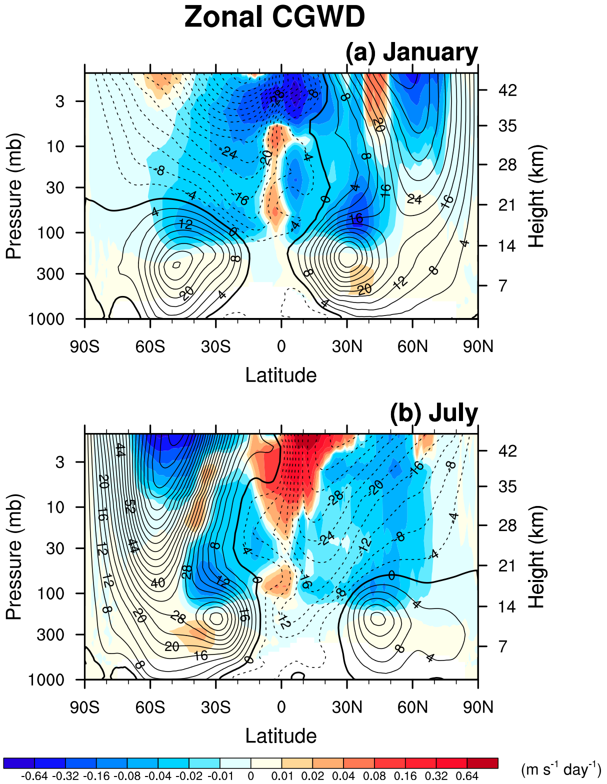

FIG. 2. Latitude–height cross sections of the zonal-mean zonal wind (contour lines) and the CGWD (shaded) in (a) January and (b) July averaged from 1979 to 2010. Positive (negative) zonal winds are plotted with solid (dashed) lines, and thick contour lines denote a zero zonal wind speed.

Figure 2 shows latitude–height cross sections of the zonal-mean zonal wind (contour lines) and CGWD (shading) in January (Fig. 2a) and July (Fig. 2b). The magnitude of the CGWD is generally less than 1 m s^{-1} day^{-1}, and the values of the maximum and minimum CGWD in January (July) in the stratosphere are 0.1 (1.5) and -0.9 (-0.7) m s^{-1} day^{-1} at 45°N (12°N) and 6°N (56°S), respectively. During January (Fig. 2a), there is a strong negative drag in the upper stratosphere over the equatorial region under the easterly background wind. That is, easterly wind is accelerated by the CGWD. In the midlatitudes of the NH, the CGWD decelerates the stratospheric jet (60°N) and accelerates the equatorward part of the stratospheric jet (40°N) above 10 hPa. The acceleration of the equatorward flank of jet occurs by competition between the westerly acceleration by dissipation of the eastward-propagating GWs through the critical-level filtering process and the easterly acceleration by dissipation of the westward-propagating

GWs through the wave saturation process, resulting in net positive CGWD in the upper stratosphere (Fig. S1 in the online supplemental material). The westerly acceleration in the westerly background condition through the critical-level filtering process is possible here, because the CGW parameterization considered in the present study has a wide phase speed spectrum ranging from -80 to $+80\,\mathrm{m\,s^{-1}}$. In the midlatitude regions of the SH (summer hemisphere), the CGWD accelerates the easterly wind in the stratosphere, because the stronger westward momentum flux over the midlatitude regions (30°–60°N) in the summer hemisphere at 100 hPa decreases continuously with height, whereas the eastward momentum flux is nearly invariable with the height (Fig. 1). With the exception of the equatorial region, the magnitude and sign of CGWD are similar in July (Fig. 2b) in consideration of the seasonal hemispheric changes. In contrast, the CGWD in the upper stratosphere near the equator (Fig. 2b) is mostly positive in July; in January, however, a strong negative drag exists. This is because the 32-yr average leads to the additional inclusion of positive (negative) shear cases between 30 and 3 hPa in July (January) because of the asymmetric inclusion of QBO phases. Furthermore, GWs dissipate not only through the critical-level filtering process but also by wave breaking in the upper stratosphere, where the wave amplitude is large enough to saturate. In July, the CGWMF is dominantly positive at the source level and is saturated more strongly near the stratopause than in January (not shown), resulting in a strong positive CGWD.

Although the sign of the CGWD is different between January and July, the largest CGWD can be found in the tropical upper stratosphere in both months. The magnitude of the CGWD in the upper stratosphere (above ~40 km) over the tropical region is 0.5–$1\,\mathrm{m\,s^{-1}\,day^{-1}}$ on average. The magnitude of the momentum forcing in ERA-Interim required for driving the SAO is approximately 1–$2\,\mathrm{m\,s^{-1}\,day^{-1}}$ (Fig. 1 of Ern et al. 2015) in the altitude range of 40–45 km. This implies that the CGWD contributes significantly to the momentum forcing required for driving the SAO in the tropical upper stratosphere. This is consistent with previous studies that SAO structure extends down to the upper stratosphere, which is closer to the observed SAO structure (Garcia et al. 1997), after including a physically based CGW parameterization into a GCM (Beres et al. 2005; Song et al. 2007). The zonal CGWD and zonal wind in both January and July of each year are given in the supplemental material (Fig. S2). Figure S2 shows a larger magnitude of the CGWD in the lower stratosphere than Fig. 2, because the sign of the CGWD changes significantly from year to year. The meridional CGWMF (Fig. S3) and CGWD (Fig. S4) are also given in the supplemental material.

Figure 3 shows the power spectrum of the CGWMF with respect to the horizontal wavenumber k_h and the vertical wavenumber m in five latitudinal bands (45°–75°N, 15°–45°N, 15°N–15°S, 15°–45°S, and 45°–75°S) at the cloud top and at 100, 50, and 10 hPa in January (Fig. 3a) and July (Fig. 3b). At the cloud top (see also Fig. 4 of Part I), the CGWMF with horizontal and vertical wavelengths of 8–100 and 1–40 km, respectively, are generally dominant, and relatively strong powers at longer horizontal and vertical wavelengths are shown in the tropical region (15°N–15°S). During the propagation from the cloud top to 100 hPa, the power of the CGWMF reduces significantly, and regions of strong spectral powers shift to shorter vertical wavelengths because of the high static stability in the stratosphere. The spectral powers at short vertical wavelengths ($\lambda_z < 5$ km) are slightly reduced at 50 hPa, and the CGWs with λ_z between 1 and 2 km almost disappear at 10 hPa because of the dissipation of short-wavelength components. As a result, spectral powers at horizontal wavelengths from 8 to 100 km (from 8 to 100 km) and vertical wavelengths from 1 to 20 km (from 3 to 30 km) at 50 hPa (10 hPa) are pronounced in the current study. Those scales of GWs cannot be resolved from most current GCMs, including high-resolution ones with horizontal grid spacing of 0.25° (Preusse et al. 2014), and thus, they should be parameterized in GCMs, before some of those CGWs are explicitly resolved from GCMs in the future, probably with a horizontal grid spacing of a few kilometers. The GWs with these horizontal and vertical wavelengths are similar to those observed from SPBs near 50 hPa in the tropical region (λ_h from 1 to 50 km; Jewtoukoff et al. 2013) but are very different from those observed by limb sounder (λ_h longer than ~200 km and λ_z from 4 to 16 km; Wright et al. 2015) and nadir-scanning instruments (λ_h longer than 30–80 km and λ_z greater than 15 km; Ern et al. 2017).

In July (Fig. 3b), the shape of the power spectrum is quite similar to that in January (Fig. 3a), but the overall magnitude is larger in July than in January because of the less-pronounced filtering in the stratosphere. It is interesting that there are three spectral peaks at 15°–45° in the summer hemisphere at 100 hPa. The first peak at small wavelengths (λ_h between 10 and 20 km and λ_z between 3 and 10 km) is part of the strong westward waves at 30°–60° in the summer hemisphere. The second and third peaks mainly represent waves from the latitude band between 0° and 30° in the summer hemisphere. These separate peaks appear because a strong easterly shear in the summer hemisphere starting from the altitude of 200 hPa filters out westward ($c < 0$) waves at small phase speeds. The stronger peak ($\lambda_h \sim 80$ km and $\lambda_z \sim 15$ km) corresponds to eastward-moving

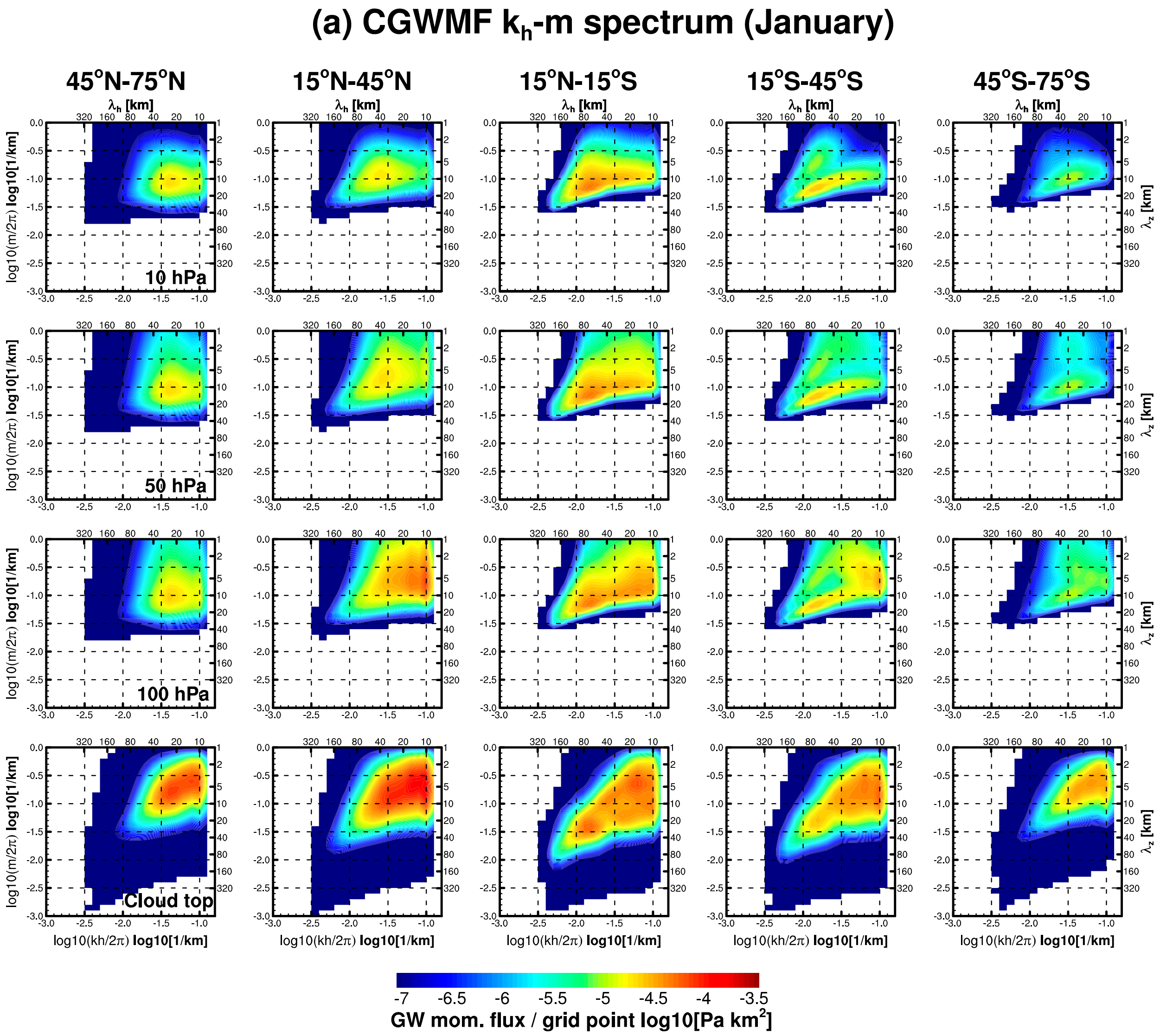

FIG. 3. The 32-yr (1979–2010)-averaged CGWMF magnitude with respect to the horizontal wavelength (x axis) and the vertical wavelength (y axis) averaged over (left to right) 45°–75°N, 15°–45°N, 15°N–15°S, 15°–45°S, and 45°–75°S at (bottom to top) the cloud top, 100, 50, and 10 hPa in (a) January and (b) July.

waves, and the weaker peak ($\lambda_h \sim 60$ km and $\lambda_z \sim 5$ km) corresponds to westward waves with a high phase speed.

Figure 4 shows the phase speed spectrum of the CGWMF at 50 hPa (10°S, 60°E) on 15 February 2010. This location and time is selected for a comparison with the phase speed spectrum of GWs observed from SPBs (Jewtoukoff et al. 2013). We select 315° counterclockwise from east, which is one of the propagation angles in the current parameterization and is similar to the wave propagation angle observed from SPBs at that time (from 300° to 360°). The overall shape of the parameterized spectrum in the current study (solid line in Fig. 4a) is similar to the observed one (black line in Fig. 4b), except for phase speeds ranging from -10 to $10\,\mathrm{m\,s^{-1}}$, and it matches slightly better than the numerically simulated spectrum (red line in Fig. 4b) by Jewtoukoff et al. (2013) for phase speeds ranging from 10 to $40\,\mathrm{m\,s^{-1}}$. Jewtoukoff et al. (2013) argued that the numerically simulated wind is almost zero, which is different from the real wind, and this leads to an overestimation of the amount of the critical-level filtered momentum flux at near-zero phase speeds. Similar reasons apply to our parameterized spectrum. The mean wind from the cloud top to 50 hPa in the current study is 0–$4\,\mathrm{m\,s^{-1}}$, and the CGW spectra in this phase speed range are totally filtered out during the propagation from the cloud top to 50 hPa.

In addition, there is a possibility that waves with near-zero phase speeds propagate from other regions. We

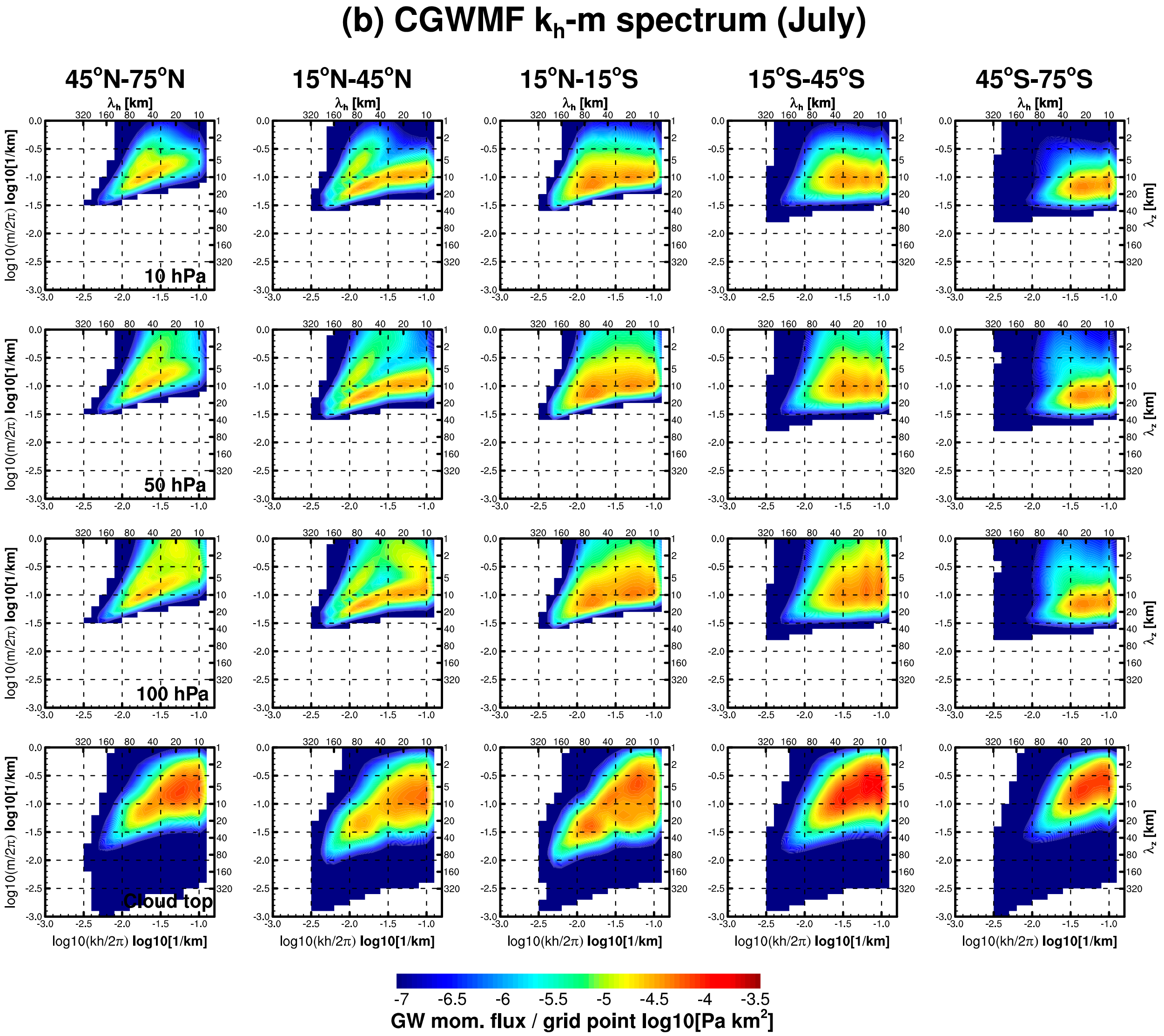

FIG. 3. (*Continued*)

examined this possibility by conducting an additional calculation on 15 February 2010 using a ray-tracing model of Song and Chun (2008) using the same source-level momentum flux spectrum. It shows (Fig. 4a) that the result with ray-tracing propagation is generally similar to that from the current columnar propagation except that the CGWMF at near-zero phase speed is increased slightly and at 15 m s^{-1} is decreased. Although this difference is not significant in its magnitude, the result from the ray-tracing calculation is closer to the observation. Given that the discrepancies between the observation and the offline calculation of CGW parameterization are significant at near-zero phase speeds, additional factors to induce those differences need to be investigated as a future research topic. A more general feature of difference in CGWD between the current columnar calculation and ray-tracing calculation are examined based on a 1-month calculation, and results will be discussed in the last section of the paper.

4. Contributions of CGWs to the QBO

Figure 5 shows the time–height cross sections of the momentum forcing obtained using parameterized convective gravity waves (P-CGWs) from the current offline calculation (Fig. 5a) and equatorial planetary waves consisting of Kelvin waves (Fig. 5b), mixed Rossby–gravity (MRG) waves (Fig. 5c), inertio-GWs (Fig. 5d), and Rossby waves (Fig. 5e) averaged over a latitude band of 5°N–5°S from 2000 to 2010. The momentum

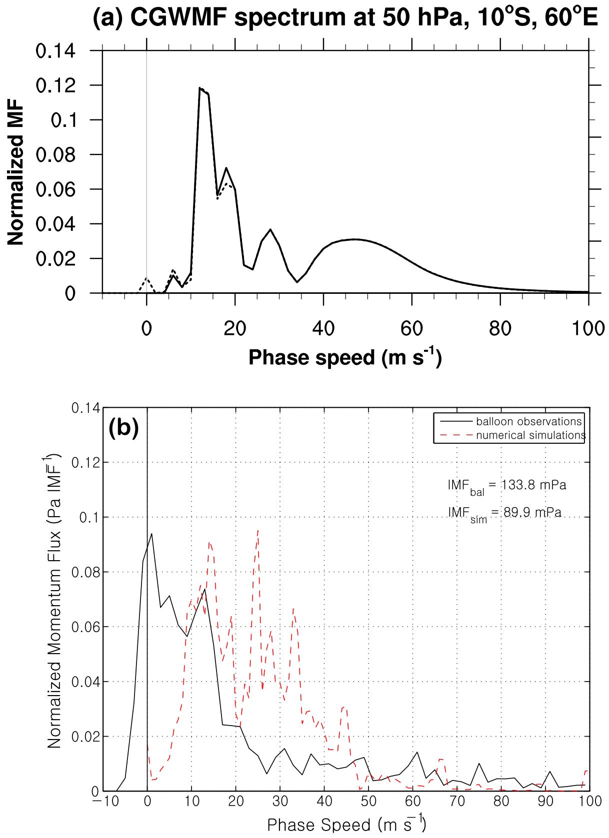

FIG. 4. (a) Phase speed spectrum of the CGWMF at a 315° propagation angle (counted counterclockwise from the east) from the columnar propagation (solid) and that from the ray-tracing propagation (dotted) at 50 hPa (10°S, 60°E) averaged on 15 Feb 2010. (b) CGWMF spectrum observed by a superpressure balloon and numerically simulated by Jewtoukoff et al. (2013). Phase speed spectrum in (b) is taken from Fig. 5 in Jewtoukoff et al. (2013). Reprinted with permission of Copyright Clearance Center. All rights reserved.

forcings by resolved equatorial planetary waves and inertio-GWs are calculated with the CFSR following the separation method by Kim and Chun (2015a,b). The details of the wave separation method are given in section 4 of Kim and Chun (2015a). Overall, the higher the altitude, the larger the CGWD because of a decrease in the air density (Fig. 5a). The magnitude of the CGW source momentum flux has strong variations and highly intermittent features (see Fig. 11 of Part I) including very large-amplitude cases, according to the strong spatiotemporal variations in convective sources and background flow that determine the CGW source spectrum. This is clearly different from the traditional nonorographic GWD parameterizations that assign a constant magnitude of source momentum flux at all model grids (or assign a latitudinally different constant). Because larger-amplitude waves can be easily saturated in the lower altitudes (Hertzog et al. 2008; de la Cámara et al. 2014; Alexander et al. 2017), CGWD in the lower stratosphere is rather large compared with the GW drag (GWD) obtained from nonorographic GW parameterizations that are not linked to the GW sources explicitly. The maximum easterly (westerly) CGW forcing at 70 hPa is -3 (2.4) m s^{-1} month^{-1}, while that at 5 hPa is -17 (30) m s^{-1} month^{-1}. It is also worthwhile to note that P-CGWs exert their momentum throughout the whole period of the QBO because of their broad spectrum, while resolved waves exert their momentum mostly at the maximum wind shear zone.

The momentum forcing by Kelvin waves has large values in the westerly shear zone with a peak of 11 m s^{-1} month^{-1} at 10 hPa (Fig. 5b). MRG waves exert negative forcings in both the westerly and the easterly shear zones (Kim and Chun 2015b), and the maximum negative forcing in the easterly shear zone is 2 m s^{-1} month^{-1} at 20 hPa. The momentum forcing by inertio-GWs is large and follows the easterly and westerly shear zones, but its magnitude is smaller and the duration of its negative forcing is shorter than those by P-CGWs. The maximum positive and negative momentum forcings by inertio-GWs are 4 and 3 m s^{-1} month^{-1}, respectively, at 5 hPa. The negative Rossby wave forcing is large both below 50 hPa during the NH winter and above 10 hPa when the QBO wind is westerly. The maximum magnitude of the negative momentum forcing by Rossby waves in the easterly shear zone is 5 m s^{-1} month^{-1} at 5 hPa. The positive forcing in the westerly shear zone is dominated by Kelvin waves (P-CGWs) below (above) 30 hPa, while the negative forcing in the easterly shear zone is dominated by P-CGWs at all altitudes.

The phase-maximum magnitudes of the momentum forcing by the resolved waves and P-CGWs at 30 hPa are shown in Table 1. The magnitude of the momentum forcing by P-CGWs is 3.5–6 m s^{-1} month^{-1}, which is comparable to but slightly smaller than that by Kelvin waves in the westerly shear zone. In the easterly shear zone, the negative forcing by P-CGWs is 3.1–6 m s^{-1} month^{-1}, which is 2–3 times larger than the westward forcing by any of the resolved equatorial waves. Kim and Chun (2015b) estimated the momentum forcing required for driving the QBO by the equatorial waves resolved from four reanalyses: ERA-Interim (ERA-I), the Modern-Era Retrospective Analysis for Research and Applications (MERRA; Rienecker et al. 2011), the CFSR, and the Japanese 55-year Reanalysis (JRA-55; Kobayashi et al. 2015), and they showed that the temporal variations in the momentum forcing by each wave type at 30 hPa are generally consistent among the reanalyses. However, the magnitude of the positive forcing by Kelvin [inertio-gravity (IG)] waves and the negative forcing by inertio-GWs and MRG

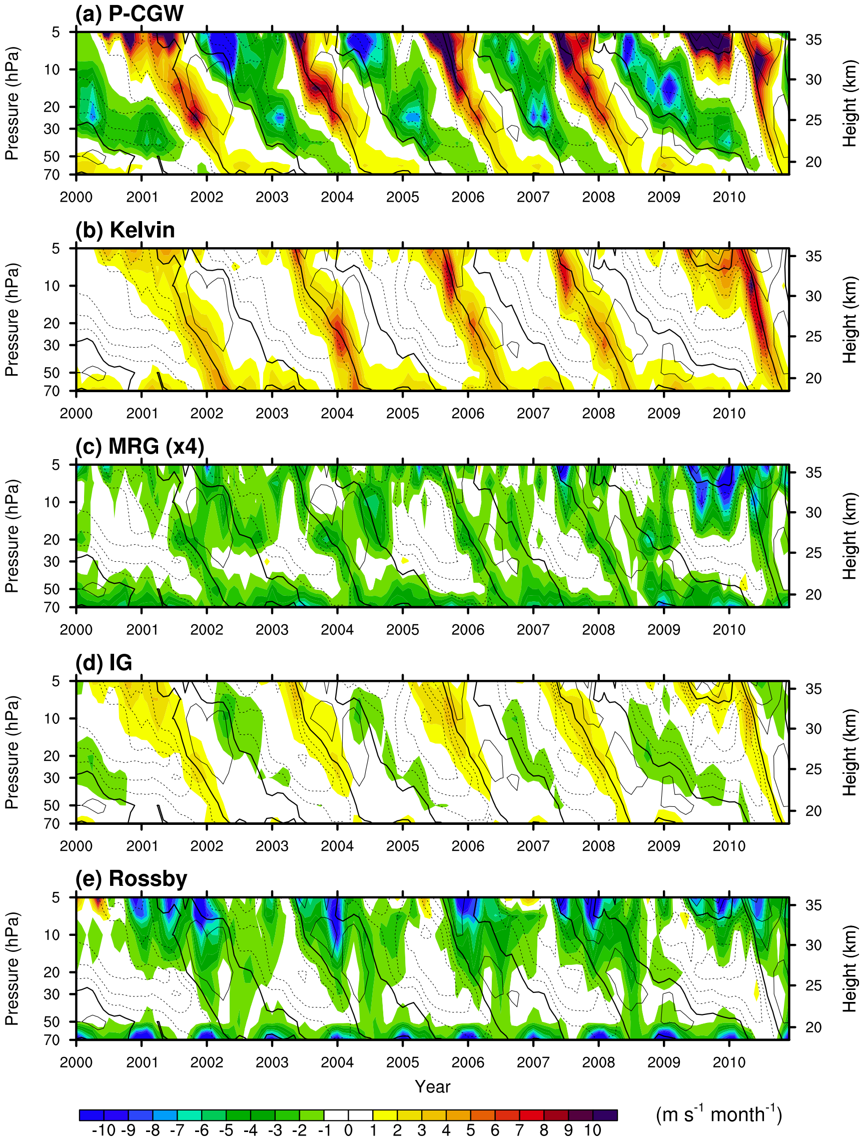

FIG. 5. Time–height cross sections of the momentum forcing (shading) by (a) P-CGWs and resolved equatorial waves, including (b) Kelvin, (c) MRG (multiplied by 4), (d) inertio-gravity, and (e) Rossby waves, superimposed with the zonal wind (contour lines) averaged over 5°N–5°S from 2000 to 2010. Positive (negative) zonal winds are plotted with solid (dashed) lines with a contour interval of 10 m s^{-1}. Thick contour lines denote a zero zonal wind speed.

(Rossby) waves from the CFSR are slightly smaller (larger) than those from other reanalyses at 30 hPa. Even considering the aforementioned differences among the reanalyses, parameterized CGWs with $\lambda_h < 100$ km contribute to the westerly shear of the QBO slightly less than Kelvin waves do, while they contribute predominantly to the easterly shear of the QBO compared with any of the resolved waves.

Kim and Chun (2015a) used the source-based CGW parameterization of Choi and Chun (2011) in HadGEM2, which is similar to the parameterization used in the present study, and thus, their results can be compared with those of the current study. The momentum forcing by parameterized CGWs from Kim and Chun (2015a) is 3–6 m s^{-1} month^{-1} for the westerly shear zone and 3–6.5 m s^{-1} month^{-1} for the easterly shear zone at 24 km (~30 hPa), both of which are quite similar to the findings of the current study. However, in addition to CGWs, a large amount of background GWs with a similar magnitude of the CGWs was needed additionally in their

TABLE 1. Phase-maximum magnitudes of the wave forcing ($\mathrm{m\,s^{-1}\,month^{-1}}$) in the CFSR, including the forcings by Kelvin, MRG, IG, and Rossby waves and the forcing by P-CGWs from an offline parameterization at 30 hPa from 1979 to 2010.

	Westerly shear	Easterly shear
Kelvin	3–7	—
MRG	—	0.2–1.2
IG	1.7–3.3	0.4–2
Rossby	—	0.7–3.5
P-CGW	3.5–6	3.1–6

model to simulate the QBO, because of underestimated resolved equatorial planetary waves and gravity waves. Therefore, total parameterized GW forcing in HadGEM2 was 8–12 (10–16) $\mathrm{m\,s^{-1}\,month^{-1}}$ for the westerly (easterly) shear zone at 24 km. Imposing a strong source-level momentum flux of GWs is probably a common feature of most GCM simulations, including any nonorographic GWD parameterizations, to reproduce the observed wind and temperature fields under the situation of underestimated planetary waves and inertio-GWs at model grids. Stronger source-level momentum flux induces stronger GWD in the stratosphere, in general. For example, the magnitude of parameterized GWD in driving the QBO in the Max Planck Institute Earth System Model is 12–18 $\mathrm{m\,s^{-1}\,month^{-1}}$ (Krismer and Giorgetta 2014) and that in the Community Atmosphere Model, version 5, is 9–12 $\mathrm{m\,s^{-1}\,month^{-1}}$ (Richter et al. 2014) in the altitude range of 20–30 hPa, which is far stronger than our estimation. That is, the magnitudes of the imposed parameterized GW momentum flux (GWMF) at the launch level and the resultant GWD in the middle atmosphere from the online simulation of a GCM may overrepresent the impacts of small-scale GWs. This motivates the current offline CGW parameterization using reanalysis data to estimate precisely the contributions of small-scale CGWs to the evolution of the QBO.

In Part I, strong annual cycle and ENSO-related variations (4–8 years) are shown in CTMF in the equatorial eastern Pacific region (see Fig. 9 of Part I), and strong spectral powers of CGWD averaged over 5°S–5°N at 30 hPa exist at 12 and 48–96 months (not shown) as well. This implies that the CGWD may have different characteristics regarding to the season, QBO phases, and ENSO phases. Figure 6 shows the monthly averaged zonal-mean eastward (westward) CGWMF at 100 hPa from 20°N to 20°S overlaid with the zonal-mean column-maximum (column minimum) zonal wind from the cloud top to 100 hPa calculated using the whole 32-yr period of data. The eastward CGWMF (Fig. 6a) exhibits a large value when the maximum zonal wind is easterly or near zero, although the shading of large CGWMF values

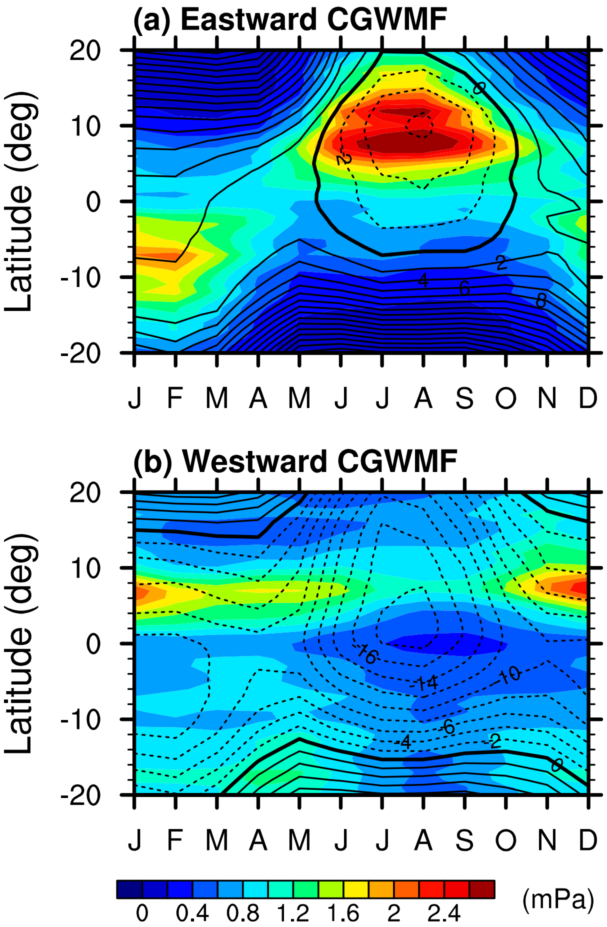

FIG. 6. Monthly averaged zonal-mean (a) eastward and (b) westward CGW momentum fluxes at 100 hPa (shading) superimposed with the zonal-mean maximum zonal wind between the cloud top and 100 hPa and minimum zonal wind between the cloud top and 100 hPa (contour lines) from 20°N to 20°S during 1979–2010. Positive (negative) zonal winds are plotted with solid (dashed) lines, and thick contour lines denote zero zonal wind speed.

and the contour line of the maximum zonal wind do not exactly match each other. The westward CGWMF (Fig. 6b) does not always display large values when the minimum zonal wind is westerly or near zero; meanwhile, there is a thin maximum layer between 0° and 10°N during the weak easterly season (from November to April). The critical-level filtering by the background wind determines the dominant wave propagation direction, resulting in seasonal changes both in the eastward and the westward CGWMF, and larger variations are observed in the eastward CGWMF. The seasonal cycle in CGWMF in the current study is generally similar to that in online simulation by Kim and Chun (2015a) except that the magnitude is much less and there are two separate peaks between 5° to 15°N during the NH summertime in Fig. 6, compared with the one peak in Fig. 6 of Kim and Chun

TABLE 2. Seasonal variations in the numbers of the EQBO and WQBO cases over 32 years (1979–2010). The EQBO and WQBO are defined by the zonal wind at 30 hPa (see text for details).

	Jan	Feb	Mar	Apr	May	Jun	Jul	Aug	Sep	Oct	Nov	Dec	Total
EQBO	10	8	9	14	14	16	15	15	16	14	13	13	157
WQBO	13	14	18	18	14	12	11	15	14	13	14	14	170

(2015a). We also calculated the CGWD at 30 hPa (not shown), and we found that there are maximum eastward and westward drags where the strong eastward and westward momentum fluxes exist at 100 hPa, respectively. This implies that the seasonal cycle of the CGWMF at the source level strongly influences the seasonal cycle of the CGWD at 30 hPa.

5. Composite analysis of the different QBO phases

Using zonal wind data from the Free University of Berlin (Naujokat 1986; http://www.geo.fu-berlin.de/en/met/ag/strat/produkte/qbo/index.html), we define the easterly QBO (EQBO) and westerly QBO (WQBO) phases when the anomaly of the monthly zonal wind from its climatological (32 yr) mean divided by its standard deviation at 30 hPa is less than −0.5 and greater than +0.5, respectively. The 30-hPa level is selected because the EQBO and WQBO phases are composed of similar numbers of months because of the relatively similar durations of the easterly and westerly phases compared with the phases at other altitudes. The numbers of the EQBO and WQBO in each month are shown in Table 2. More EQBO phases occur during the boreal summer months, while more WQBO phases occur during the boreal spring months. This implies that any composite analysis result during the EQBO and WQBO may contain a seasonal dependency.

Figure 7 shows the composite analysis of the CGWMF and CGWD during each QBO phase. It is easily seen that the primary peak of the zonal CGWMF is located at low latitudes in the NH regardless of the altitude. This can be explained by the large zonal CGWMF near 10°N throughout the year (Fig. 6). Because of the wind-filtering effect in the stratosphere, the eastward (westward) CGWMF is larger during the EQBO (WQBO), while the sum of the eastward and westward CGWMF (i.e., the absolute zonal CGWMF) is slightly larger during the EQBO. The CGWD has its maximum value at the level of maximum vertical wind shear. During the EQBO, the negative CGWD near 30 hPa extends latitudinally to ±20°, and its peak is located between 0° and 10°N. During the WQBO, however, the positive CGWD near 30 hPa is confined to 10°N–10°S, and its peak is located at the equator. This is because the source-level CGWMF is dominated by eastward waves at the equator and the positive wind shear is restricted to ±10° while the negative wind shear is extended latitudinally to ±20°. This is consistent with previous studies, which showed that westerly accelerations are more concentrated at the equator than easterly accelerations (Hamilton 1984).

To examine how the CGWMF and wind profile determine the magnitude and location of the CGWD, Fig. 8 shows the phase speed spectra of the zonal CGWMF (shading) superimposed by the zonal wind (black line) and CGWD (green line) averaged over 5°N–5°S and 5°–10°N during the EQBO and WQBO, respectively. Consistent with the zonal CGWD in Fig. 7, the negative CGWD near 30 hPa during the EQBO is larger in 5°–10°N than in 5°N–5°S. This is because the negative CGWMF spectrum near the source level (100–300 hPa) is much stronger and broader in 5°–10°N than in 5°N–5°S. Meanwhile, the positive CGWD near 30 hPa during the WQBO is larger in 5°N–5°S than in 5°–10°N, which can be observed either through the CGWD that is vertically broader in 5°N–5°S than in 5°–10°N (Fig. 7) or by the larger magnitude of the CGWD in 5°N–5°S ($1.8\,\mathrm{m\,s^{-1}\,month^{-1}}$) than in 5°–10°N ($1.1\,\mathrm{m\,s^{-1}\,month^{-1}}$; Fig. 8). This is because the positive vertical wind shear below 30 hPa is much larger in 5°N–5°S than in 5°–10°N, although the positive CGWMF near the source level is stronger in 5°–10°N than in 5°N–5°S. Referring back to Fig. 5, the maximum negative CGWD locates where zonal wind is near $-10\,\mathrm{m\,s^{-1}}$, and the maximum positive CGWD locates where zonal wind is near zero. It is because the maximum negative CGWMF is at the phase speed of $\sim -10\,\mathrm{m\,s^{-1}}$ and this can be filtered out by the easterly background wind extending to $-30\,\mathrm{m\,s^{-1}}$, whereas the peak of positive CGWMF is at $-5 < c < 10\,\mathrm{m\,s^{-1}}$ and the maximum westerly wind is generally less than $10\,\mathrm{m\,s^{-1}}$ (Fig. 8).

To investigate the dependency on the ENSO phase, we define El Niño (EL), La Niña (LA), and neutral ENSO events according to when the oceanic Niño index (ONI; http://www.cpc.ncep.noaa.gov/data/indices/oni.ascii.txt) is larger than 0.5, smaller than −0.5, and between −0.5 and 0.5, respectively. We also count the number of months when the sea surface temperature (SST) anomaly in the Niño-3.4 region is positive and negative and calculate the SST anomaly averaged in each phase. The results are shown in Table 3 along with the numbers of EL, LA, and neutral ENSO events during the EQBO and WQBO.

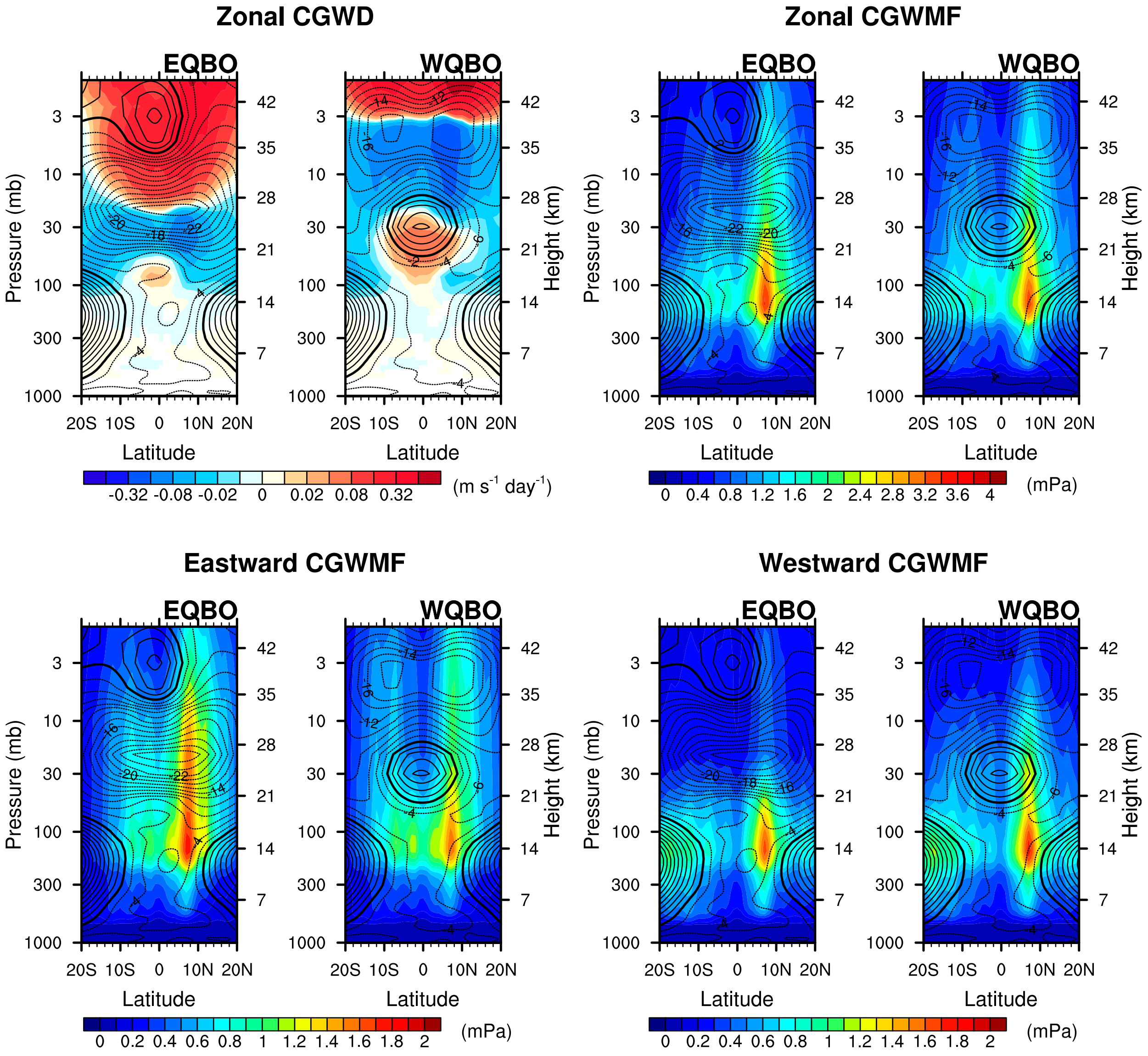

FIG. 7. Composite analysis of the (top left) zonal CGWD, (top right) zonal CGWMF, (bottom left) eastward CGWMF, and (bottom right) westward CGWMF during the EQBO and WQBO superimposed with the zonal-mean zonal wind (contour lines). EQBO and WQBO phases are defined when the anomaly of the monthly zonal wind from its climatological (32 yr) mean divided by its standard deviation at 30 hPa is less than −0.5 and greater than +0.5, respectively.

Both EL events and LA events are more frequently detected during the WQBO phase, and the number of months with a positive (negative) SST anomaly is larger during the WQBO (EQBO). This is consistent with the much stronger mean SST anomaly observed during the WQBO than during the EQBO.

Figure 9 shows the seasonal composites of the CGWMF and CGWD during the EQBO and WQBO for neutral ENSO cases. The differences in the CGWD between the EQBO and WQBO are generally similar to those in Fig. 7. An interesting feature is a seasonal variation in the CGWD both for the EQBO and for the WQBO that is associated with the seasonal variations in the zonal wind and zonal CGWMF. For the zonal wind, the wind anomaly associated with the QBO near 30 hPa changes with the season: westerly winds are shifted to the winter hemisphere during the WQBO, while easterly winds are shifted to the summer hemisphere during the EQBO. The westerly (easterly) winds of the WQBO (EQBO) are slightly shifted to the south (north) in September–November (SON), while nearly symmetric easterlies and westerlies with respect to the equator are found in March–May (MAM). For the CGWMF, regardless of the season, there is a local maximum between 5° and

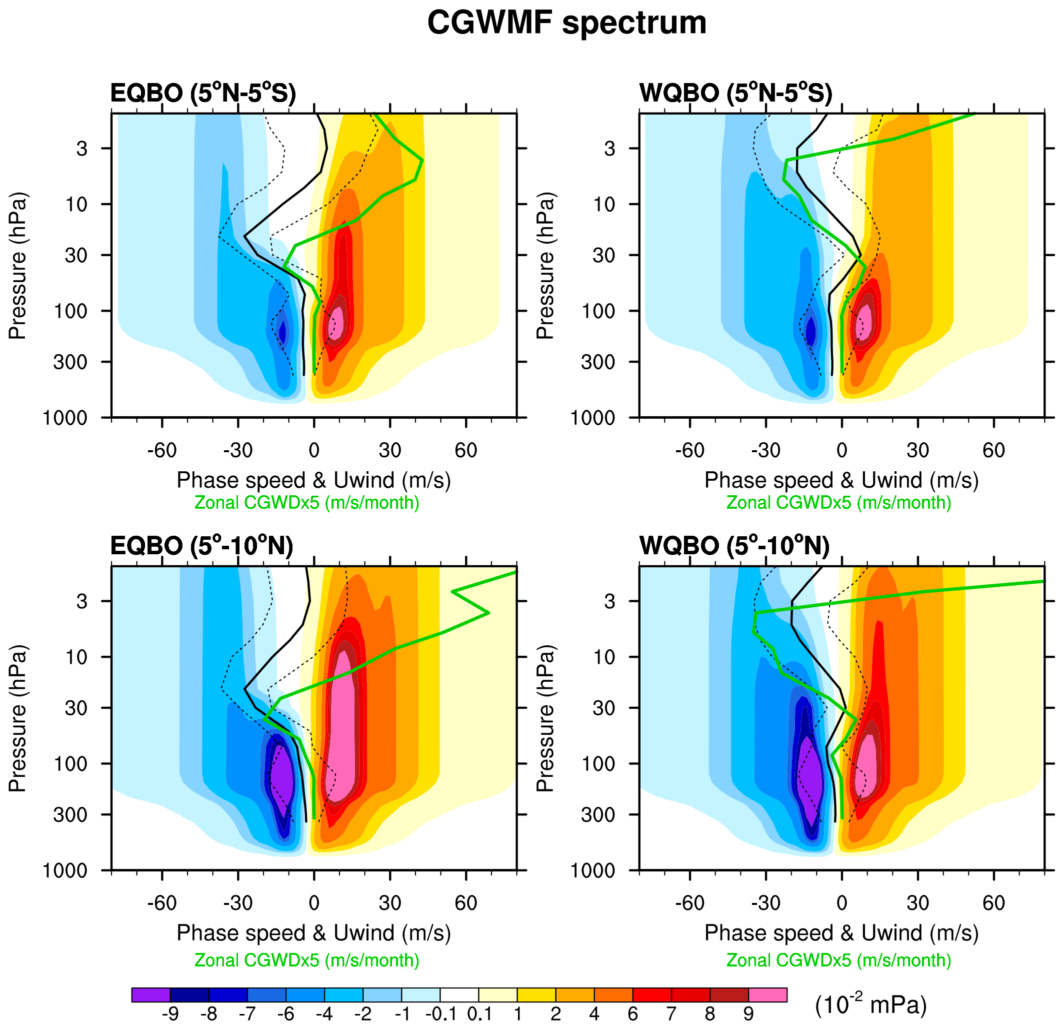

FIG. 8. Zonal CGWMF spectra from the source level (cloud top) to the stratosphere averaged over (top) 5°N–5°S and (bottom) 5°–10°N during the (left) EQBO and (right) WQBO. The black (green) solid line in each panel represents the zonal wind (zonal CGWD multiplied by a factor of 5) averaged over the same location and period, and the black dashed lines show plus and minus one standard deviation of the zonal-mean zonal wind.

10°N contributed by westward waves, and its magnitude increases during the boreal winter [December–February (DJF); Fig. 6]. Except for the peak in 5°–10°N, the CGWMF moves northward in June–August (JJA) and southward in DJF because of the north and south migration of the intertropical convergence zone (ITCZ), and this seasonal motion is contributed mostly by the eastward CGWMF (Fig. 6). The magnitude of the CGWMF is the largest during JJA (Fig. 9), with the largest contribution from eastward waves (Fig. 6).

During the WQBO, the maximum CGWMF and the maximum positive wind shear move in opposite directions. For example, the westerly and the corresponding positive vertical wind shear near 30 hPa are shifted southward (northward) while the maximum CGWMF moves northward (southward) in JJA (DJF), resulting in less coincidence between the latitudinal location where the maximum wind shear exists and that where the maximum CGWMF exists. Therefore, the positive CGWDs near 30 hPa in JJA and DJF are located closer to the summer hemisphere, although the maximum westerly wind shear is closer to the winter hemisphere. In JJA, the largest eastward momentum flux leads to the strongest positive CGWD. A comparison of the latitude-integrated positive CGWD in each season (not shown) reveals that the strongest (weakest) positive CGWD occurs during JJA (MAM) near 30 hPa during the WQBO.

During the EQBO, the negative CGWD near 30 hPa does not show any seasonal north and south migration because the seasonal movement of the CGWMF related to the ITCZ is less evident for westward waves (Fig. 6).

TABLE 3. (second to fourth columns) Numbers of EL, LA, and neutral ENSO events during the EQBO and WQBO phases over 32 years (1979–2010). EL, LA, and neutral ENSO are defined when the ONI is larger than 0.5, smaller than −0.5, and between −0.5 and 0.5, respectively, and the mean SST anomaly (°C) in each period is shown in parentheses. (fifth column),(sixth column) The number of months for the positive and negative SST anomalies in the Niño-3.4 region during the EQBO and WQBO phases and (seventh column) the SST anomaly averaged in each phase are also shown.

Niño-3.4 region	EL (mean SST)	LA (mean SST)	Neutral (mean SST)	Positive SST	Negative SST	Mean SST
EQBO	36 (0.98)	30 (−0.82)	91 (−0.03)	74	83	4.7×10^{-2}
WQBO	45 (1.14)	40 (−1.02)	85 (0.02)	94	75	7.5×10^{-2}

Although the source-level CGWMF is the smallest in MAM, the magnitude of the negative CGWD near 30 hPa is greater than that in any other season because of the maximum coincidence of the locations of the maximum wind shear and maximum CGWMF. The latitude-integrated negative CGWD is the strongest (weakest) during MAM (SON) near 30 hPa during the EQBO. DJF shows a strong negative CGWD in the upper stratosphere both in the EQBO and in the WQBO, which is different from other seasons, and this strong CGWD above the ~35 km might be related to SAO, as mentioned in Fig. 2.

While we focus only on the neutral ENSO case in Fig. 9, we show the EL and LA composites and the differences between them during DJF in Fig. 10. For the EL (LA) composites, 10 (10) EQBO and 10 (13) WQBO cases are used. During EL, the zonal CGWMF is strong across 10°N–20°S. During LA, the latitudinal extents of the regions with a strong momentum flux are roughly similar to those during EL, but the CGWMF is stronger in 5°–10°N and weaker near the equator. In the difference plot (Fig. 10c), the zonal CGWMF is larger between 6°N and 6°S during EL and larger poleward of 6° during LA. Statistically significant differences at the 95% confidence level using a *t* test (Wilks 2006) exist below 300 hPa as well as all altitudes poleward of 6°N during the EQBO and all altitudes equatorward of 6° during WQBO. Although statistically insignificant, the larger CGWMF values between 10° and 25°S during LA are consistent with the recently observed GWMF at an altitude of 39 km by AIRS (Sato et al. 2016). They showed that the maximum precipitation moving southward during LA is mainly responsible for the large CGWMF observed therein. The larger CGWMF near the equator during EL is also consistent with the arguments provided by Geller et al. (2016b).

The CGWD patterns during EL and LA are similar to each other during DJF and are not much different from

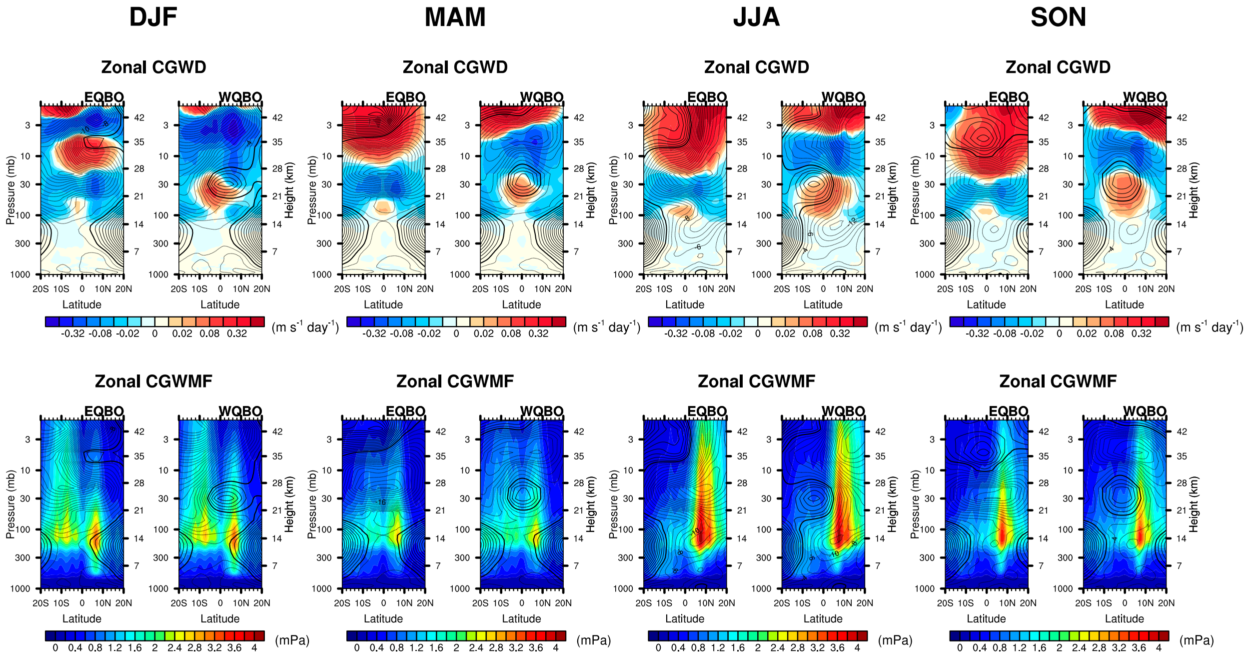

FIG. 9. As in Fig. 7, except the composite is performed in each season—(left to right) DJF, MAM, JJA, and SON—for neutral ENSO events and only the zonal CGWD and zonal CGWMF are shown.

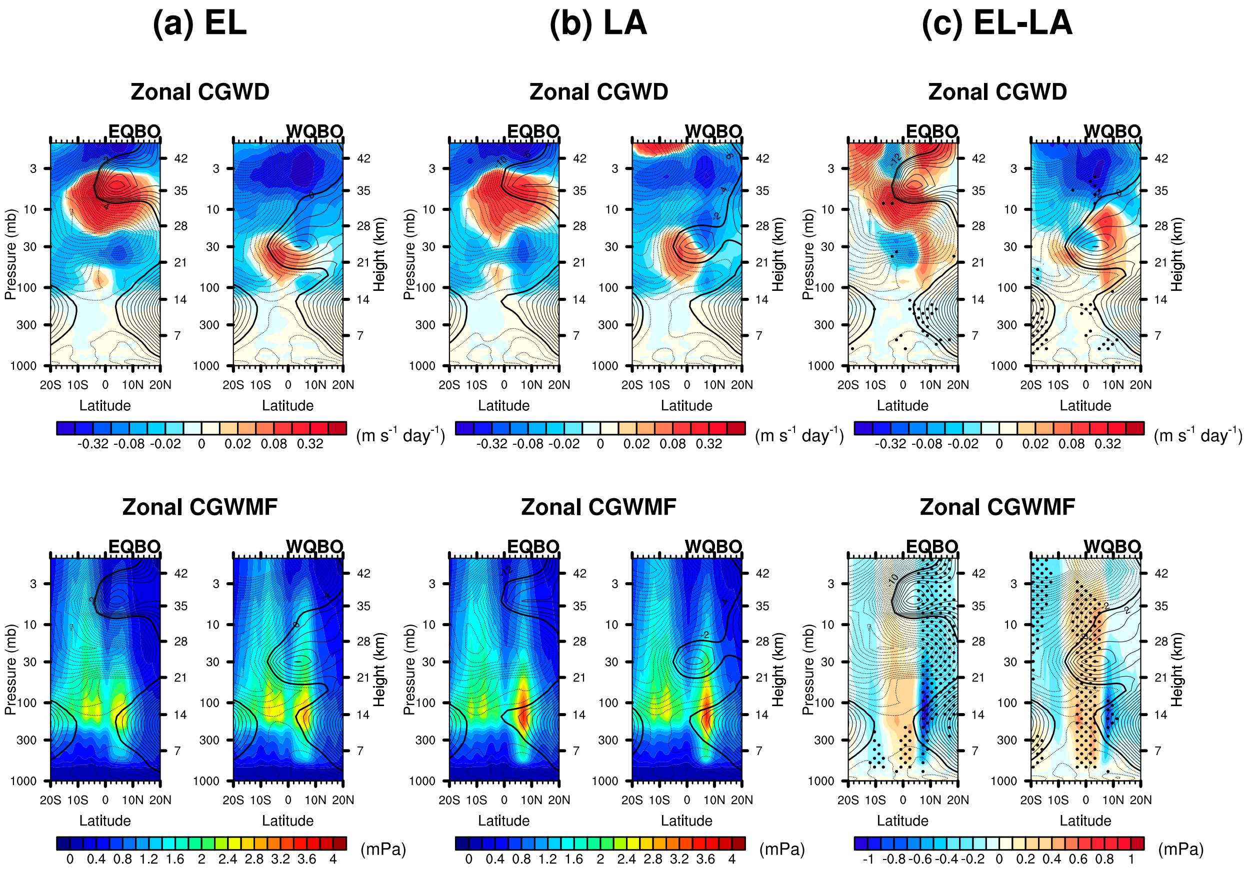

FIG. 10. As in Fig. 9, except the composite is performed for (a) EL, (b) LA, and (c) the differences between the two (EL − LA) during DJF. Composite of the zonal-mean zonal wind (contour lines) during EL (LA) is superimposed onto the CGWD (shading) during EL and EL − LA (LA). The dotted pattern represents a statistically significant difference at the 95% confidence level using a *t* test.

those for the neutral ENSO case during those months (Fig. 9). However, there is a notable difference in the CGWD magnitude between EL and LA (Fig. 10c). The CGWD over 6°N–6°S, where the CGWMF is larger during EL, has a magnitude in the stratosphere that is generally stronger during EL than during LA. A larger CGWD implies a faster propagation rate of the QBO during EL, which is consistent with the previous studies conducted by Taguchi (2010) and Yuan et al. (2014) using radiosonde observations. Schirber (2015) also showed a faster propagation rate of the QBO during EL using a GCM with a physically based CGW source spectrum and attributed it to both a larger resolved wave forcing and a parameterized CGW forcing during EL. The stronger CGWD over 6°N–6°S during EL is partly due to the stronger vertical wind shear during EL. In the composite results (Fig. 10), the QBO amplitude (i.e., the amplitude of the zonal wind) is generally larger during EL than during LA. This is somewhat different from the results by Taguchi (2010) and Yuan et al. (2014), who showed that the QBO amplitude is larger during LA than during EL based on tropical radiosonde data and EOF analysis. Their EOF analyses were based on wind data from 10 to 70 hPa, and thus, an altitude at which the amplitude actually increases is difficult to identify. The modeling study by Schirber (2015) revealed that the increase in the amplitude during EL depends on both the time and the altitude: for the EQBO phase, the strength of the westerly jet is increased in the first half of the simulation and decreased in the second half of the simulation during EL, whereas the easterly jet underlying the westerly jet is always larger during LA. Note that the EQBO and WQBO phases of Taguchi (2010) are nearly similar to those based on the 50-hPa zonal wind (see Fig. 2 of Taguchi 2010). When we additionally perform the QBO composite analysis based on the 50-hPa zonal wind (not shown), we obtain a consistent result (i.e., a larger QBO amplitude during LA than during EL). This implies that the amplitude increases during different ENSO phases vary with both the time and the height.

Figure 11 shows the phase speed spectra of the zonal CGWMF at 100 hPa averaged over 5°N–5°S in the

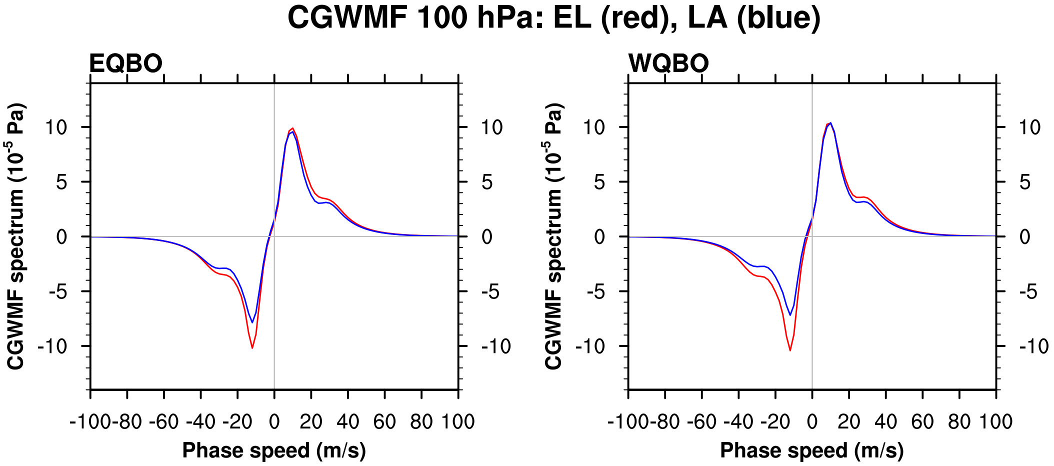

FIG. 11. Phase speed spectrum of the zonal CGWMF averaged over 5°N–5°S at 100 hPa during EL (red) and LA (blue) in the (left) EQBO and (right) WQBO.

EQBO and WQBO phases during EL and LA during the whole 32 years (1979–2010). The larger magnitude of the CGWMF during EL is pronounced in the phase speed range between -20 and $-5\,\mathrm{m\,s^{-1}}$ and noticeable in the phase speed range of ± 20–$40\,\mathrm{m\,s^{-1}}$ both in the EQBO and in the WQBO. This can be explained by the convective activities that are generally stronger during EL than during LA. The modeling study by Schirber (2015) also showed a larger and broader source-level CGW spectrum during EL. Meanwhile, it was recently suggested that deep convection patterns are observed more frequently during LA than during EL (Geller et al. 2016b; Alexander et al. 2017), leading to a broader CGW spectrum that results in a relatively larger QBO amplitude during LA (Geller et al. 2016a). In our dataset, neither frequently occurring deep convections nor broader CGW spectrum during LA compared to EL is found, which needs further investigation in the future.

6. Summary and discussion

In this study, the characteristics of the stratospheric convective gravity wave momentum flux (CGWMF) and the convective gravity wave drag (CGWD) are examined using an offline physically based CGW parameterization by Part I with a Lindzen-type columnar wave propagation scheme. First, we examined the global characteristics of the CGWMF and the effects of the CGWMF on large-scale circulation in terms of the CGWD. Then we investigated the contributions of small-scale CGWs to the quasi-biennial oscillation (QBO) and the characteristics of CGWs during different QBO phases, seasons, and ENSO. The current study focuses on small-scale CGWs generated by an individual mesoscale convective cell that are mostly unresolved from recent satellite observations and high-resolution modeling data. The dominant horizontal wavelengths of CGWs considered in the present study range from 8 to 100 km at both 50 and 10 hPa, and the vertical wavelengths range from 1 (3) to 20 (30) km at 50 (10) hPa. The phase speed spectrum of the CGWMF matches well with the GWMF spectrum observed by superpressure balloons (SPBs) in the tropical region.

The CGWMF has two peaks: one in the summer hemisphere tropics (dominated by eastward waves) and another at midlatitude regions in the winter hemisphere (dominated by westward waves) in the stratosphere. Several peaks of the CGWMF, for example, over the northern Atlantic Ocean and the Norwegian coast, exist in January at 3 hPa, which is consistent with previous studies (e.g., Preusse et al. 2014). The Asian summer monsoon region has a large eastward CGWMF at the source level, and it extends up to 3 hPa in July. This unfiltered momentum flux likely contributes to the (i) driving of the westerly shear of the stratopause SAO and (ii) eastward GWD forcing near the mesopause that contributes to the driving of the one-cell meridional gyre in the mesosphere. The CGWD (averaged over 32 years) is the most prominent in the upper stratosphere in tropical regions and at midlatitude regions in the wintertime in both January and July (Fig. 2). The CGWD in the tropical upper stratosphere may contribute to the driving of the SAO with a magnitude of 0.5–$1\,\mathrm{m\,s^{-1}\,day^{-1}}$ above ~40 km. The stratospheric jet (~60°) in the winter hemisphere is decelerated by the CGWD, but it is accelerated at the equatorward flank of the jet.

CGWs provide a momentum forcing to the westerly shear of the QBO (3.5–$6\,\mathrm{m\,s^{-1}\,month^{-1}}$) that is significant but smaller than the forcing by Kelvin waves, while CGWs can provide a greater momentum forcing to the easterly shear of the QBO (3.1–6 $\mathrm{m\,s^{-1}\,month^{-1}}$) than any other equatorial waves (Table 1). Composite analyses of the zonal CGWMF and CGWD during the EQBO and WQBO phases, which are selected based on the 30-hPa zonal wind, are investigated under different seasons and ENSO phases. The primary peak of the zonal CGWMF is located at low latitudes in the NH because of the large CGWMF at 100 hPa near 10°N throughout the year (Fig. 6) both in the EQBO and in the WQBO. During the EQBO, the negative CGWD near 30 hPa extends to ±20°, and its peak is located between 0° and 10°N. During the WQBO, the positive CGWD near 30 hPa is confined to 10°N–10°S, which is caused by the location of the source-level CGWMF and vertical wind shear. Seasonally, the largest eastward CGWMF is located at low latitudes in the NH (SH) in JJA (DJF), and the largest westward CGWMF is located at low latitudes in the NH in DJF. The strongest negative CGWD is in MAM during the EQBO, and the strongest positive CGWD is in JJA during the WQBO near 30 hPa. The location of the maximum CGWD moves with time, and its latitude follows the north–south migration of the ITCZ. The positive and negative drags in both the EQBO and the WQBO are larger during El Niño (EL) than during La Niña (LA) events, especially over 6°N–6°S. This is caused by not only a larger magnitude of the zonal CGWMF but also a strong wind shear during EL.

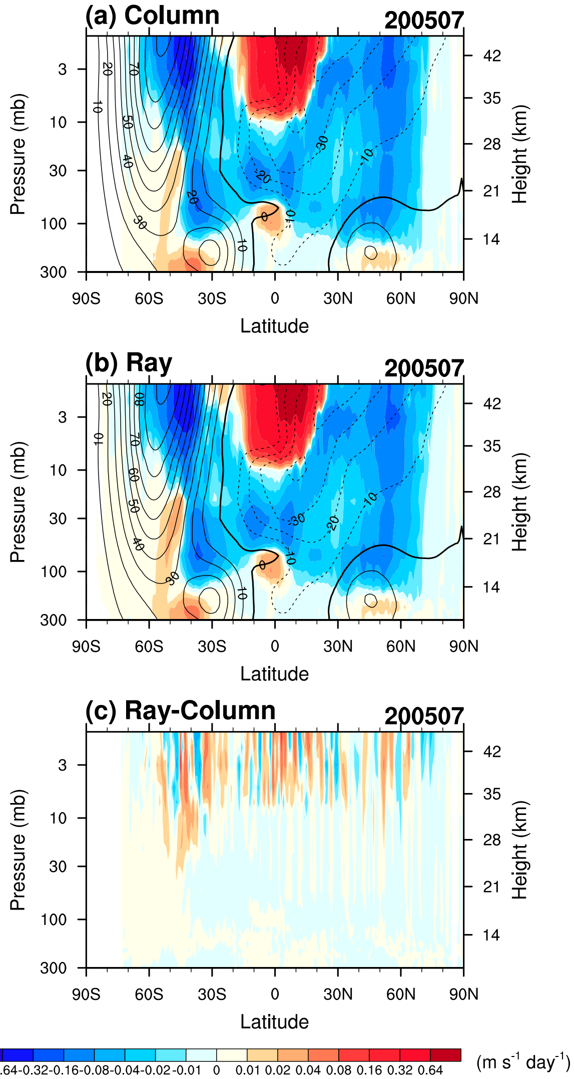

FIG. 12. Latitude–height cross sections of the zonal-mean zonal CGWD (shading) and zonal wind (contour) for July 2005 calculated by (a) columnar and (b) ray-based propagation using the ray-tracing model by Song and Chun (2008). (c) The difference between (a) and (b) (shading).

The current results are based on the offline CGW parameterization using global reanalysis data, and some uncertainties may be included in the parameterization and reanalysis data. The potential factors that could lead to uncertainties in the source-level CGW parameterization were discussed in depth in Part I. One additional point to mention is on the Lindzen-type columnar propagation scheme used in this study. Ray-based CGWD parameterizations have been used in previous modeling studies (e.g., Song and Chun 2008; Choi and Chun 2013) and offline studies (e.g., Choi et al. 2012; Trinh et al. 2016; Kalisch et al. 2016), but we could not consider ray-tracing wave propagation into our study because of the considerable computational costs (hourly calculation for 32 years in the whole stratosphere). To examine the differences in CGWD between column-based and ray-based wave propagation, additional calculation using the ray-based wave propagation by Song and Chun (2008) is conducted for one month in July 2005, and the result is shown in Fig. 12. Note that the column-based calculation is conducted using Song and Chun's (2008) ray-tracing model by turnoff horizontal propagation, which is generally the same as in the current columnar calculation (see Fig. S2) except that CGWD is calculated at the vertical level where wind is calculated and the vertical wave reflection is considered when the vertical wavelengths are longer than 100 km. The ray-tracing model of Song and Chun (2008) allows horizontal propagation of each ray, while the horizontal wavenumbers are not changed following the ray. It shows that two results are very similar with a difference of less than 10% in most areas. CGWD is slightly smaller in ray-based calculation near the polar night jet where strong vertical wind shear exists, and the negative CGWD in the NH and SH high latitudes (poleward of ±60°) near the stratopause is shifted to the poleward compared to column-based calculation. In the tropical region, positive CGWD is slightly stronger above an altitude of 10 hPa in ray-based calculation, while the difference is negligible below 10 hPa. We performed an additional ray-tracing calculation using Gravity Wave Regional or Global Ray Tracer (GROGRAT; Marks and Eckermann 1995) that includes horizontal wave refraction with the full dispersion relationship and different saturation scheme (Fritts and Rastogi 1985). The results of column-based and ray-based calculation by GROGRAT (not shown) are very similar, with a difference less than 10% in most areas, as in Fig. 12. The small differences between the columnar and ray-tracing calculation from the two ray-tracing calculations likely stem from the fact that the CGWs considered in the present study with small horizontal wavelengths and high frequencies propagate vertically rather than horizontally, and wave reflection and horizontal refraction are not significant, especially in the tropical stratosphere where QBO is involved. This confirms the current results with the columnar propagation.

Two additional considerations must be mentioned with regard to the uncertainties in the global reanalysis data used in the current study. First, the zonal wind in the tropical region is less accurate because fewer in situ measurement data are assimilated within the tropical region. This is also represented by the large spread of the zonal wind in recent reanalysis data (Podglajen et al. 2014; Kawatani et al. 2016). Because wave propagation and dissipation are controlled largely by the wind and wind shear in the tropical region, the accuracy of the wind in the reanalysis dataset is important for the present study. Second, as mentioned previously in Part I, there are uncertainties in the convective heating rate and in the cloud-top and cloud-bottom information provided by the CFSR, which are generally model-produced data. In particular, the depth of convective heating is important for determining the dominant vertical wavelength through the resonance between the natural mode and convective forcing (Song and Chun 2005).

In this study, we examined the impacts of small-scale GWs ($\lambda_h < 100$ km) on the zonal wind in the stratosphere and estimated their contributions to the QBO using an offline calculation of physically based CGW parameterization using hourly global reanalysis data for 32 years for the first time. The CGWs considered in this study are neither observed from satellites nor simulated from high-resolution GCMs, although the contributions of those CGWs to the momentum budget in the middle atmosphere are significant. In addition, our results would give some insights into understanding the variations in CGWD for driving the QBO regarding to the seasonal and ENSO phases. The results of the 32-yr time series of hourly CGWMF and CGWD data from the cloud top to the upper stratosphere can be utilized in many research fields, including (i) GCM simulations to constrain the magnitude of the GWMF at the source level and in the stratosphere, (ii) research on the Madden–Julian oscillation (MJO) in conjunction with the QBO (e.g., Kalisch et al. 2018), (iii) improvements to our understanding of cycle-to-cycle variations in the QBO wind structure, and (iv) as a tropospheric source spectrum of GWD parameterization included in a GCM that extends to the upper thermosphere, in the study of migrating diurnal tide–GW interaction in the mesosphere and thermosphere (e.g., Yiğit and Medvedev 2017). Some interesting research topics, including the poleward propagation of CGWs during the summertime and the QBO amplitude with respect to different ENSO phases, remain to be investigated in the near future.

Acknowledgments. This work was funded by the Korea Meteorological Administration Research and Development Program under Grant KMIPA 2015-6160. The NCEP CFSR data were downloaded from the Research Data Archive at the National Center for Atmospheric Research, Computational and Information Systems Laboratory, Boulder, Colorado (available online at https://doi.org/10.5065/D69K487J), and from the National Ocean and Atmospheric Administration (NOAA) National Operational Model Archive and Distribution System, National Climatic Data Center, Asheville, North Carolina (available online at http://nomads.ncdc.noaa.gov/modeldata/cmd_pgbh/).

REFERENCES

Alexander, M. J., and J. R. Holton, 1997: A model study of zonal forcing in the equatorial stratosphere by convectively induced gravity waves. *J. Atmos. Sci.*, **54**, 408–419, https://doi.org/10.1175/1520-0469(1997)054<0408:AMSOZF>2.0.CO;2.

——, D. A. Ortland, A. W. Grimsdell, and J.-E. Kim, 2017: Sensitivity of gravity wave fluxes to interannual variations in tropical convection and zonal wind. *J. Atmos. Sci.*, **74**, 2701–2716, https://doi.org/10.1175/JAS-D-17-0044.1.

Andrews, D. G., J. R. Holton, and C. B. Leovy, 1987: *Middle Atmosphere Dynamics.* Academic Press, 489 pp.

Anstey, J. A., J. F. Scinocca, and M. Keller, 2016: Simulating the QBO in an atmospheric general circulation model: Sensitivity to resolved and parameterized forcing. *J. Atmos. Sci.*, **73**, 1649–1665, https://doi.org/10.1175/JAS-D-15-0099.1.

Baldwin, M. P., and Coauthors, 2001: The quasi-biennial oscillation. *Rev. Geophys.*, **39**, 179–229, https://doi.org/10.1029/1999RG000073.

Beres, J. H., R. R. Garcia, B. A. Boville, and F. Sassi, 2005: Implementation of a gravity wave source spectrum parameterization dependent on the properties of convection in the Whole Atmosphere Community Climate Model (WACCM). *J. Geophys. Res.*, **110**, D10108, https://doi.org/10.1029/2004JD005504.

Butchart, N., and Coauthors, 2018: Overview of experiment design and comparison of models participating in phase 1 of the SPARC Quasi-Biennial Oscillation initiative (QBOi). *Geosci.*

Model Dev., **11**, 1009–1032, https://doi.org/10.5194/gmd-11-1009-2018.

Choi, H.-J., and H.-Y. Chun, 2008: Effects of vertical resolution on a parameterization of convective gravity waves. *Atmosphere*, **18**, 121–136.

——, and ——, 2011: Momentum flux spectrum of convective gravity waves. Part I: An update of a parameterization using mesoscale simulations. *J. Atmos. Sci.*, **68**, 739–759, https://doi.org/10.1175/2010JAS3552.1.

——, and ——, 2013: Effects of convective gravity wave drag in the Southern Hemisphere winter stratosphere. *J. Atmos. Sci.*, **70**, 2120–2136, https://doi.org/10.1175/JAS-D-12-0238.1.

——, ——, and I.-S. Song, 2007: Characteristics and momentum flux spectrum of convectively forced internal gravity waves in ensemble numerical simulations. *J. Atmos. Sci.*, **64**, 3723–3734, https://doi.org/10.1175/JAS4037.1.

——, ——, J. Gong, and D. L. Wu, 2012: Comparison of gravity wave temperature variances from ray-based spectral parameterization of convective gravity wave drag with AIRS observations. *J. Geophys. Res.*, **117**, D05115, https://doi.org/10.1029/2011JD016900.

Chun, H.-Y., I.-S. Song, and T. Horinouchi, 2005: Momentum flux spectrum of convectively forced gravity waves: Can diabatic forcing be a proxy for convective forcing? *J. Atmos. Sci.*, **62**, 4113–4120, https://doi.org/10.1175/JAS3610.1.

——, H.-J. Choi, and I.-S. Song, 2008: Effects of nonlinearity on convectively forced internal gravity waves: Application to a gravity wave drag parameterization. *J. Atmos. Sci.*, **65**, 557–575, https://doi.org/10.1175/2007JAS2255.1.

——, Y.-H. Kim, H.-J. Choi, and J.-Y. Kim, 2011: Influence of gravity waves in the tropical upwelling: WACCM simulations. *J. Atmos. Sci.*, **68**, 2599–2612, https://doi.org/10.1175/JAS-D-11-022.1.

Dee, D. P., and Coauthors, 2011: The ERA-Interim reanalysis: Configuration and performance of the data assimilation system. *Quart. J. Roy. Meteor. Soc.*, **137**, 553–597, https://doi.org/10.1002/qj.828.

de la Cámara, A., F. Lott, and A. Hertzog, 2014: Intermittency in a stochastic parameterization of nonorographic gravity waves. *J. Geophys. Res. Atmos.*, **119**, 11 905–11 919, https://doi.org/10.1002/2014JD022002.

Dunkerton, T. J., 1997: The role of gravity waves in the quasi-biennial oscillation. *J. Geophys. Res.*, **102**, 26 053–26 076, https://doi.org/10.1029/96JD02999.

——, and D. P. Delisi, 1985: Climatology of the equatorial lower stratosphere. *J. Atmos. Sci.*, **42**, 376–396, https://doi.org/10.1175/1520-0469(1985)042<0376:COTELS>2.0.CO;2.

Ern, M., and P. Preusse, 2009: Quantification of the contribution of equatorial Kelvin waves to the QBO wind reversal in the stratosphere. *Geophys. Res. Lett.*, **36**, L21801, https://doi.org/10.1029/2009GL040493.

——, ——, J. C. Gille, C. L. Hepplewhite, M. G. Mlynczak, J. M. Russell III, and M. Riese, 2011: Implications for atmospheric dynamics derived from global observations of gravity wave momentum flux in stratosphere and mesosphere. *J. Geophys. Res.*, **116**, D19107, https://doi.org/10.1029/2011JD015821.

——, and Coauthors, 2014: Interaction of gravity waves with the QBO: A satellite perspective. *J. Geophys. Res. Atmos.*, **119**, 2329–2355, https://doi.org/10.1002/2013JD020731.

——, P. Preusse, and M. Riese, 2015: Driving of the SAO by gravity waves as observed from satellite. *Ann. Geophys.*, **33**, 483–504, https://doi.org/10.5194/angeo-33-483-2015.

——, L. Hoffmann, and P. Preusse, 2017: Directional gravity wave momentum fluxes in the stratosphere derived from high-resolution AIRS temperature data. *Geophys. Res. Lett.*, **44**, 475–485, https://doi.org/10.1002/2016GL072007.

Evan, S., M. J. Alexander, and J. Dudhia, 2012: WRF simulations of convectively generated gravity waves in opposite QBO phases. *J. Geophys. Res.*, **117**, D12117, https://doi.org/10.1029/2011JD017302.

Fritts, D. C., and P. K. Rastogi, 1985: Convective and dynamical instabilities due to gravity wave motions in the lower and middle atmosphere: Theory and observations. *Radio Sci.*, **20**, 1247–1277, https://doi.org/10.1029/RS020i006p01247.

——, and M. J. Alexander, 2003: Gravity wave dynamics and effects in the middle atmosphere. *Rev. Geophys.*, **41**, 1003, https://doi.org/10.1029/2001RG000106.

Garcia, R. R., T. J. Dunkerton, R. S. Lieberman, and R. A. Vincent, 1997: Climatology of the semiannual oscillation of the tropical middle atmosphere. *J. Geophys. Res.*, **102**, 26 019–26 032, https://doi.org/10.1029/97JD00207.

Geller, M. A., and Coauthors, 2016a: Modeling the QBO—Improvements resulting from higher-model vertical resolution. *J. Adv. Model. Earth Syst.*, **8**, 1092–1105, https://doi.org/10.1002/2016MS000699.

——, T. Zhou, and W. Yuan, 2016b: The QBO, gravity waves forced by tropical convection, and ENSO. *J. Geophys. Res. Atmos.*, **121**, 8886–8895, https://doi.org/10.1002/2015JD024125.

Giorgetta, M. A., E. Manzini, E. Roeckner, M. A. Esch, and L. Bengtsson, 2006: Climatology and forcing of the quasi-biennial oscillation in the MAECHAM5 model. *J. Climate*, **19**, 3882–3901, https://doi.org/10.1175/JCLI3830.1.

Hamilton, K., 1984: Mean wind evolution through the quasi-biennial cycle of the tropical lower stratosphere. *J. Atmos. Sci.*, **41**, 2113–2125, https://doi.org/10.1175/1520-0469(1984)041<2113:MWETTQ>2.0.CO;2.

Hertzog, A., C. Souprayen, and A. Hauchecorne, 2001: Observation and backward trajectory of an inertio-gravity wave in the lower stratosphere. *Ann. Geophys.*, **19**, 1141–1155, https://doi.org/10.5194/angeo-19-1141-2001.

——, G. Boccara, R. A. Vincent, and F. Vial, 2008: Estimation of gravity wave momentum flux and phase speeds from quasi-Lagrangian stratospheric balloon flights. Part II: Results from the Vorcore campaign in Antarctica. *J. Atmos. Sci.*, **65**, 3056–3070, https://doi.org/10.1175/2008JAS2710.1.

Holt, L. A., M. J. Alexander, L. Coy, A. Molod, W. Putman, and S. Pawson, 2016: Tropical waves and the quasi-biennial oscillation in a 7-km global climate simulation. *J. Atmos. Sci.*, **73**, 3771–3783, https://doi.org/10.1175/JAS-D-15-0350.1.

Holton, J. R., 1983: The influence of gravity wave breaking on the general circulation of the middle atmosphere. *J. Atmos. Sci.*, **40**, 2497–2507, https://doi.org/10.1175/1520-0469(1983)040<2497:TIOGWB>2.0.CO;2.

——, and R. S. Lindzen, 1972: An updated theory for the quasi-biennial cycle of the tropical stratosphere. *J. Atmos. Sci.*, **29**, 1076–1080, https://doi.org/10.1175/1520-0469(1972)029<1076:AUTFTQ>2.0.CO;2.

Huesmann, A. S., and M. H. Hitchman, 2001: The stratospheric quasi-biennial oscillation in the NCEP reanalyses: Climatological structures. *J. Geophys. Res.*, **106**, 11 859–11 874, https://doi.org/10.1029/2001JD900031.

Jewtoukoff, V., R. Plougonven, and A. Hertzog, 2013: Gravity waves generated by deep tropical convection: Estimates from balloon observations and mesoscale simulations. *J. Geophys. Res. Atmos.*, **118**, 9690–9707, https://doi.org/10.1002/jgrd.50781.

Kalisch, S., H.-Y. Chun, M. Ern, P. Preusse, Q. T. Trinh, S. D. Eckermann, and M. Riese, 2016: Comparison of simulated and observed convective gravity waves. *J. Geophys. Res. Atmos.*, **121**, 13 474–13 492, https://doi.org/10.1002/2016JD025235.

——, M.-J. Kang, and H.-Y. Chun, 2018: Impact of convective gravity waves on the tropical middle atmosphere during the Madden-Julian oscillation. *J. Geophys. Res. Atmos.*, https://doi.org/10.1029/2017JD028221, in press.

Kang, M.-J., H.-Y. Chun, and Y.-H. Kim, 2017: Momentum flux of convective gravity waves derived from an offline gravity wave parameterization. Part I: Spatiotemporal variations at source level. *J. Atmos. Sci.*, **74**, 3167–3189, https://doi.org/10.1175/JAS-D-17-0053.1.

Kawatani, Y., S. Watanabe, K. Sato, T. J. Dunkerton, S. Miyahara, and M. Takahashi, 2010: The roles of equatorial trapped waves and internal inertia–gravity waves in driving the quasi-biennial oscillation. Part I: Zonal mean wave forcing. *J. Atmos. Sci.*, **67**, 963–980, https://doi.org/10.1175/2009JAS3222.1.

——, K. Hamilton, K. Miyazaki, M. Fujiwara, and J. A. Anstey, 2016: Representation of the tropical stratospheric zonal wind in global atmospheric reanalyses. *Atmos. Chem. Phys.*, **16**, 6681–6699, https://doi.org/10.5194/acp-16-6681-2016.

Kim, J.-E., and M. J. Alexander, 2013: Tropical precipitation variability and convectively coupled equatorial waves on submonthly time scales in reanalyses and TRMM. *J. Climate*, **26**, 3013–3030, https://doi.org/10.1175/JCLI-D-12-00353.1.

Kim, Y.-H., and H.-Y. Chun, 2015a: Contributions of equatorial wave modes and parameterized gravity waves to the tropical QBO in HadGEM2. *J. Geophys. Res. Atmos.*, **120**, 1065–1090, https://doi.org/10.1002/2014JD022174.

——, and ——, 2015b: Momentum forcing of the quasi-biennial oscillation by equatorial waves in recent reanalyses. *Atmos. Chem. Phys.*, **15**, 6577–6587, https://doi.org/10.5194/acp-15-6577-2015.

——, A. C. Bushell, D. R. Jackson, and H.-Y. Chun, 2013: Impacts of introducing a convective gravity-wave parameterization upon the QBO in the Met Office Unified Model. *Geophys. Res. Lett.*, **40**, 1873–1877, https://doi.org/10.1002/grl.50353.

Kim, Y.-J., S. D. Eckermann, and H.-Y. Chun, 2003: An overview of the past, present and future of gravity-wave drag parametrization for numerical climate and weather prediction models. *Atmos.–Ocean*, **41**, 65–98, https://doi.org/10.3137/ao.410105.

Kobayashi, S., and Coauthors, 2015: The JRA-55 Reanalysis: General specifications and basic characteristics. *J. Meteor. Soc. Japan*, **93**, 5–48, https://doi.org/10.2151/jmsj.2015-001.

Krismer, T. R., and M. A. Giorgetta, 2014: Wave forcing of the quasi-biennial oscillation in the Max Planck Institute Earth System Model. *J. Atmos. Sci.*, **71**, 1985–2006, https://doi.org/10.1175/JAS-D-13-0310.1.

——, ——, and M. Esch, 2013: Seasonal aspects of the quasi-biennial oscillation in the Max Planck Earth System Model and ERA-40. *J. Adv. Model. Earth Syst.*, **5**, 406–421, https://doi.org/10.1002/jame.20024.

Lane, T. P., M. J. Reeder, and T. L. Clark, 2001: Numerical modeling of gravity wave generation by deep tropical convection. *J. Atmos. Sci.*, **58**, 1249–1274, https://doi.org/10.1175/1520-0469(2001)058<1249:NMOGWG>2.0.CO;2.

Lindzen, R. S., 1981: Turbulence and stress owing to gravity wave and tidal breakdown. *J. Geophys. Res.*, **86**, 9707–9714, https://doi.org/10.1029/JC086iC10p09707.

——, and J. R. Holton, 1968: A theory of the quasi-biennial oscillation. *J. Atmos. Sci.*, **25**, 1095–1107, https://doi.org/10.1175/1520-0469(1968)025<1095:ATOTQB>2.0.CO;2.

Marks, C. J., and S. D. Eckermann, 1995: A three-dimensional nonhydrostatic ray-tracing model for gravity waves: Formulation and preliminary results for the middle atmosphere. *J. Atmos. Sci.*, **52**, 1959–1984, https://doi.org/10.1175/1520-0469(1995)052<1959:ATDNRT>2.0.CO;2.

Martin, G. M., and Coauthors, 2011: The HadGEM2 family of Met Office Unified Model climate configurations. *Geosci. Model Dev.*, **4**, 723–757, https://doi.org/10.5194/gmd-4-723-2011.

Naujokat, B., 1986: An update of the observed quasi-biennial oscillation of the stratospheric winds over the tropics. *J. Atmos. Sci.*, **43**, 1873–1877, https://doi.org/10.1175/1520-0469(1986)043<1873:AUOTOQ>2.0.CO;2.

Onogi, K., and Coauthors, 2007: The JRA-25 Reanalysis. *J. Meteor. Soc. Japan*, **85**, 369–432, https://doi.org/10.2151/jmsj.85.369.

Orr, A., P. Bechtold, J. Scinocca, M. Ern, and M. Janiskova, 2010: Improved middle atmosphere climate and forecasts in the ECMWF model through a nonorographic gravity wave drag parameterization. *J. Climate*, **23**, 5905–5926, https://doi.org/10.1175/2010JCLI3490.1.

O'Sullivan, D., 1997: Interaction of extratropical Rossby waves with westerly quasi-biennial oscillation winds. *J. Geophys. Res.*, **102**, 19 461–19 469, https://doi.org/10.1029/97JD01524.

Podglajen, A., A. Hertzog, R. Plougonven, and N. Žagar, 2014: Assessment of the accuracy of (re)analyses in the equatorial lower stratosphere. *J. Geophys. Res. Atmos.*, **119**, 11 166–11 188, https://doi.org/10.1002/2014JD021849.

Preusse, P., M. Ern, P. Bechtold, S. D. Eckermann, S. Kalisch, Q. T. Trinh, and M. Riese, 2014: Characteristics of gravity waves resolved by ECMWF. *Atmos. Chem. Phys.*, **14**, 10 483–10 508, https://doi.org/10.5194/acp-14-10483-2014.

Richter, J. H., A. Solomon, and J. T. Bacmeister, 2014: On the simulation of the quasi-biennial oscillation in the Community Atmosphere Model, version 5. *J. Geophys. Res. Atmos.*, **119**, 3045–3062, https://doi.org/10.1002/2013JD021122.

Rienecker, M. R., and Coauthors, 2011: MERRA: NASA's Modern-Era Retrospective Analysis for Research and Applications. *J. Climate*, **24**, 3624–3648, https://doi.org/10.1175/JCLI-D-11-00015.1.

Saha, S., and Coauthors, 2010: NCEP Climate Forecast System Reanalysis. *Bull. Amer. Meteor. Soc.*, **91**, 1015–1057, https://doi.org/10.1175/2010BAMS3001.1.

Sato, K., S. Watanabe, Y. Kawatani, Y. Tomikawa, K. Miyazaki, and M. Takahashi, 2009: On the origins of mesospheric gravity waves. *Geophys. Res. Lett.*, **36**, L19801, https://doi.org/10.1029/2009GL039908.

——, C. Tsuchiya, M. J. Alexander, and L. Hoffmann, 2016: Climatology and ENSO-related interannual variability of gravity waves in the Southern Hemisphere subtropical stratosphere revealed by high-resolution AIRS observations. *J. Geophys. Res. Atmos.*, **121**, 7622–7640, https://doi.org/10.1002/2015JD024462.

Scaife, A. A., N. Butchart, and C. D. Warner, 2000: Realistic quasi-biennial oscillations in a simulation of the global climate. *Geophys. Res. Lett.*, **27**, 3481–3484, https://doi.org/10.1029/2000GL011625.

Schirber, S., 2015: Influence of ENSO on the QBO: Results from an ensemble of idealized simulations. *J. Geophys. Res. Atmos.*, **120**, 1109–1122, https://doi.org/10.1002/2014JD022460.

——, E. Manzini, and M. J. Alexander, 2014: A convection-based gravity wave parameterization in a general circulation model: Implementation and improvements on the QBO. *J. Adv. Model. Earth Syst.*, **6**, 264–279, https://doi.org/10.1002/2013MS000286.

Skamarock, W. C., 2004: Evaluating mesoscale NWP models using kinetic energy spectra. *Mon. Wea. Rev.*, **132**, 3019–3032, https://doi.org/10.1175/MWR2830.1.

——, 2011: Kinetic energy spectra and model filters. *Numerical Techniques for Global Atmospheric Models*, P. H. Lauritzen et al., Eds., Lecture Notes in Computational Science and Engineering Series, Vol. 80, Springer, 495–512.

Song, I.-S., and H.-Y. Chun, 2005: Momentum flux spectrum of convectively forced internal gravity waves and its application to gravity wave drag parameterization. Part I: Theory. *J. Atmos. Sci.*, **62**, 107–124, https://doi.org/10.1175/JAS-3363.1.

——, and ——, 2006: A spectral parameterization of convectively forced internal gravity waves and estimation of gravity-wave momentum forcing to the middle atmosphere. *J. Korean Meteor. Soc.*, **42**, 339–359.

——, and ——, 2008: A Lagrangian spectral parameterization of gravity wave drag induced by cumulus convection. *J. Atmos. Sci.*, **65**, 1204–1224, https://doi.org/10.1175/2007JAS2369.1.

——, ——, and T. P. Lane, 2003: Generation mechanisms of convectively forced internal gravity waves and their propagation to the stratosphere. *J. Atmos. Sci.*, **60**, 1960–1980, https://doi.org/10.1175/1520-0469(2003)060<1960:GMOCFI>2.0.CO;2.

——, ——, R. R. Garcia, and B. A. Boville, 2007: Momentum flux spectrum of convectively forced internal gravity waves and its application to gravity wave drag parameterization. Part II: Impacts in a GCM (WACCM). *J. Atmos. Sci.*, **64**, 2286–2308, https://doi.org/10.1175/JAS3954.1.

Taguchi, M., 2010: Observed connection of the stratospheric quasi-biennial oscillation with El Niño–Southern Oscillation in radiosonde data. *J. Geophys. Res.*, **115**, D18120, https://doi.org/10.1029/2010JD014325.

——, and K. Shibata, 2013: Diagnosis of annual synchronization of the quasi-biennial oscillation: Results from JRA-25/JCDAS Reanalysis and MRI Chemistry-Climate Model data. *J. Meteor. Soc. Japan*, **91**, 243–256, https://doi.org/10.2151/jmsj.2013-301.

Thurairajah, B., D. E. Siskind, S. M. Bailey, J. N. Carstens, J. M. Russell III, and M. G. Mlynczak, 2017: Oblique propagation of monsoon gravity waves during the Northern Hemisphere 2007 summer. *J. Geophys. Res. Atmos.*, **122**, 5063–5075, https://doi.org/10.1002/2016JD026008.

Trinh, Q. T., S. Kalisch, P. Preusse, M. Ern, H.-Y. Chun, S. D. Eckermann, M.-J. Kang, and M. Riese, 2016: Tuning of a convective gravity wave source scheme based on HIRDLS observations. *Atmos. Chem. Phys.*, **16**, 7335–7356, https://doi.org/10.5194/acp-16-7335-2016.

Wallace, J. M., R. L. Panetta, and J. Estberg, 1993: Representation of the equatorial stratospheric quasi-biennial oscillation in EOF phase space. *J. Atmos. Sci.*, **50**, 1751–1762, https://doi.org/10.1175/1520-0469(1993)050<1751:ROTESQ>2.0.CO;2.

Wang, J., W. Wang, X. Fu, and K.-H. Seo, 2012: Tropical intraseasonal variability in the CFSR. *Climate Dyn.*, **38**, 2191–2207, https://doi.org/10.1007/s00382-011-1087-0.

Wei, J., and F. Zhang, 2014: Mesoscale gravity waves in moist baroclinic jet–front systems. *J. Atmos. Sci.*, **71**, 929–952, https://doi.org/10.1175/JAS-D-13-0171.1.

——, ——, and J. H. Richter, 2016: An analysis of gravity wave spectral characteristics in moist baroclinic jet–front systems. *J. Atmos. Sci.*, **73**, 3133–3155, https://doi.org/10.1175/JAS-D-15-0316.1.

Wilks, D. S., 2006: *Statistical Methods in the Atmospheric Sciences*. Academic Press, 676 pp.

Wright, C. J., S. M. Osprey, and J. C. Gille, 2015: Global distributions of overlapping gravity waves in HIRDLS data. *Atmos. Chem. Phys.*, **15**, 8459–8477, https://doi.org/10.5194/acp-15-8459-2015.

Xue, X.-H., H.-L. Liu, and X.-K. Dou, 2012: Parameterization of the inertial gravity waves and generation of the quasi-biennial oscillation. *J. Geophys. Res.*, **117**, D06103, https://doi.org/10.1029/2011JD016778.

Yiğit, E., and A. S. Medvedev, 2017: Influence of parameterized small-scale gravity waves on the migrating diurnal tide in Earth's thermosphere. *J. Geophys. Res. Space Phys.*, **122**, 4846–4864, https://doi.org/10.1002/2017JA024089.

Yuan, W., M. A. Geller, and P. T. Love, 2014: ENSO influence on QBO modulations of the tropical tropopause. *Quart. J. Roy. Meteor. Soc.*, **140**, 1670–1676, https://doi.org/10.1002/qj.2247.